UC San Diego

UC San Diego Electronic Theses and Dissertations

Title

Helium and Carbon Isotope Systematics in Groundwaters along the Southern San Andreas Fault System

Permalink

https://escholarship.org/uc/item/9p74h10q

Author

Evans, Tyler John

Publication Date

2013

Peer reviewed|Thesis/dissertation

UNIVERISTY OF CALIFORNIA, SAN DIEGO

Helium and Carbon Isotope Systematics in Groundwaters along the Southern San
Andreas Fault System

A Thesis submitted in partial satisfaction of the requirements
for the degree of Master of Science

in

Earth Sciences

by

Tyler John Evans

Committee in charge:

      Professor David Hilton, Chair
      Professor James Day
      Professor Michael Tryon

2013

The thesis of Tyler John Evans is approved and it is acceptable in
quality and form for publication on microfilm and electronically:

_____

_____

_____

Chair

University of California, San Diego

2013

TABLE OF CONTENTS

LIST OF FIGURES

LIST OF TABLES

ACKNOWLEDGEMENTS

Abstract of the Thesis

Helium and Carbon Isotope Systematics in Groundwaters along the Southern San Andreas Fault System

by

Tyler John Evans

Master of Science in Earth Sciences

University of California, San Diego 2013

Professor David Hilton, Chair

In this study, 38 groundwater wells and hotsprings were sampled in three different areas (Salton Sea, Coachella Valley, and San Bernardino) along the southernmost portion of the San Andreas Fault System (SAFS) and analyzed for helium and carbon abundances and isotopic signatures. Concentrations of ^{4}He in the groundwaters, corrected for air saturated water contributions, vary from 0.32 to 55.0 (x 10^{-7} cm^3 STP/g H$_2$O). Concentrations of CO$_2$ in the groundwaters vary from 2.62 to

38.4 (x 10^{-2} cm^3 STP/g H$_2$O). ^{3}He/^{4}He ratios vary from 0.18 to 2.23 R$_A$ (where R$_A$ = air ^{3}He/^{4}He), with Salton Sea, Coachella Valley and San Bernardino containing median ^{3}He/^{4}He ratios of 1.17 R$_A$, 0.64 R$_A$, and 1.37 R$_A$, respectively. CO$_2$/^{3}He ratios vary from 3.06 to 200 (x 10^{10}) and δ^{13}C (CO$_2$) values range from -16.8 ‰ to -4.6 (vs PDB).

Using flux calculations developed by Kennedy et al. (1997), the Salton Sea, Coachella Valley, and San Bernardino segments of the fault have calculated fluid flux rates of 1190 mm/year, 395 mm/year, and 622 mm/year, respectively. Total ^{3}He fluxes in Salton Sea (segment length 80 km), Coachella Valley (100 km), and San Bernardino (50 km) are 0.013 mol ^{3}He/year, 0.0058 mol ^{3}He/year, and 0.0050 mol ^{3}He/year, respectively. Using these calculated flux estimates and CO$_2$/^{3}He ratios, this report makes a comparison between Mid Ocean Ridge and SAFS carbon fluxes. The Salton Trough represents a transition zone between the East Pacific Rise-related CO$_2$ degassing and SAFS fault-related degassing. This report shows a positive correlation between mantle involvement and earthquake activity.

1. Introduction

The San Andreas Fault System (SAFS) is a ~1300 km-long transform fault in California. It is the most active fault system in the continental USA and has had many large and significant earthquakes within recorded history, most notably: Fort Tejon (M=7.9; 1857), Imperial Valley (M=7.8; 1892; M=7.1; 1940), San Francisco (M=7.8; 1906), Loma Prieta (M=6.9; 1989), Landers (Mojave) (M=7.3; 1992), Northridge (M=6.7; 1993), Hector Mine (Mojave) (M=7.1; 1999), and Mexicali (M=7.2; 2010) (U.S. Geological Survey, 2013). The SAFS is divided into three primary sections: northern, central, and southern. The northern section of the SAFS (~570 km) starts at the Mendocino Triple junction and ends roughly around the Monterey Bay area. The central portion of the SAFS (~400 km) continues from Monterey Bay to just north of the Big Bend section of the SAFS. Finally, the southern section (~330 km) extends from the Big Bend section to where the SAFS terminates at the southern end of the Salton Sea. The northern and southern segments of the fault are characterized by large earthquakes throughout history (up to M = 7.9), while the central segment is chiefly dominated by aseismic fault movement (Yeats, 2012). This study focuses on the southern portion of the fault.

There are roughly 30 million people who live near the fault and any significant activity along the fault could be extremely destructive. Understanding the processes and mechanisms that occur during earthquakes could help alleviate some of the risks with living near such an active fault.

One way that many have tried to understand fault activity is through direct sampling of hot springs and groundwater wells along the fault for chemical tracers, like helium or carbon isotopes (Helgeson, 1968; Kennedy et al., 1997; Furi et al., 2009; Barry et al., 2009; Onderdonk et al., 2011; Wiersberg and Erzinger, 2011; Kulongoski et al., 2013). The study of helium is of particular interest because helium isotopes (helium-3 and helium-4) are sensitive to crustal and mantle mixing so it is ideal for analysis. Additionally, isotopic analysis of CO_2 has been shown to be useful in determining origin of this volatile along the SAFS, which can lead to further conclusions of the behavior of the fault (Kennedy et al., 1997). Once the origins of these volatiles are determined, one can make a comparison of mantle involvement to recent earthquake activity. Understanding the relationship of recent earthquake activity to mantle involvement could prove to be very important in the prediction of potential hazardous segments of the SAFS.

In this study, the helium and CO_2 abundances and isotopic characteristics of groundwater collected are reported from wells close to the southern SAFS and northernmost expression of the San Jacinto Fault Zone (SJFZ) (within 10 km of a fault trace). The aims of this study are to (1) assess and explain the amount of mantle involvement within groundwaters along fault using $^3He/^4He$ ratios, (2) categorize and understand potential helium variability previously observed along the SAFS (Kennedy et al., 1997; Kulongoski et al., 2013), (3) determine the provenance of the CO_2 within the groundwaters, (4) estimate flux of CO_2 and ^3He released along the SAFS for comparison with previous studies and other mantle-volatile pathways, and (5) to

determine the relationship between volatile fluxes and earthquake activity along the southern SAFS.

2. Geology

2.1. Tectonic Setting:

The SAFS delineates the boundary between the Pacific and North American plates (Wallace, 1990). It is ~1300 km long and began formation following a change from subduction to transform motion along with the propagation of the Mendocino Triple Junction (Wallace, 1990). The SAFS consists of the San Andreas Fault (SAF) and several major branches, including the San Jacinto and Elsinore faults in southern California. The SAFS trends about N 65-70° W and has a slip rate of ~35 mm a^{-1} (Hill et al, 1990). There is an estimated ~50 mm a^{-1} relative motion between the North American and Pacific plates trending at N 35° dextral slip motion.

The San Jacinto Fault Zone (SJFZ) diverges from the SAFS northwest of Cajon Canyon between the San Gabriel and San Bernardino mountains and terminates along the southwest side of the Salton Trough (Figure 2.1.1). This ~230 km fault extends southward from the Big Bend section of the SAFS at roughly S 225° E. The two most active strands of the SJFZ are the Coyote Creek and Clark faults, which are located roughly 10 km apart. The average slip rate of the SJFZ is ~13 mm a^{-1} (Blisnuik et al., 2010).
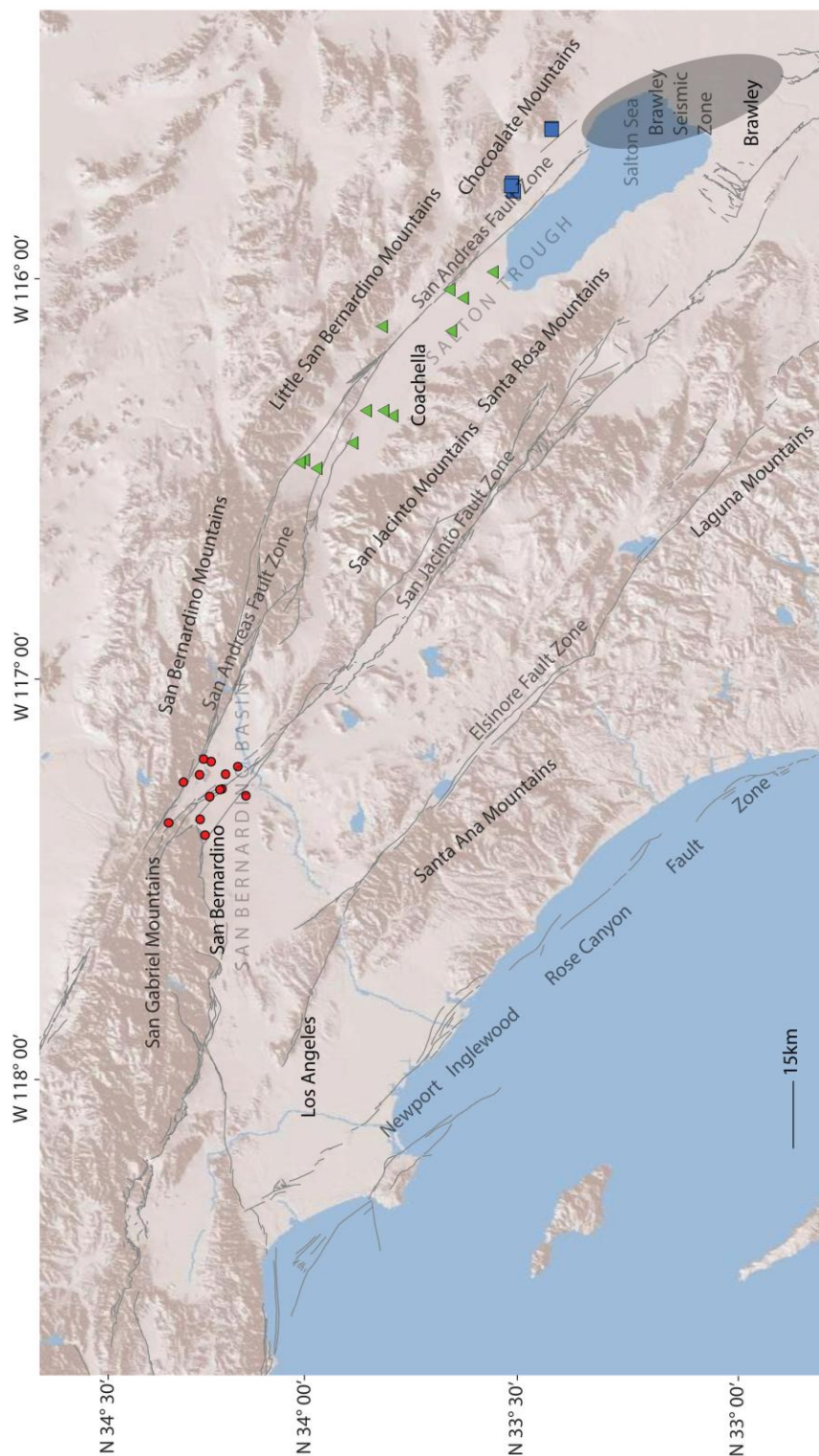
Figure 2.1.1: Map of entire study area with major mountain ranges, faults, and other features labeled. All sample locations are depicted on map. Blue squares represent Salton Sea samples, green triangles represent Coachella Valley samples, and red circles represent San Bernardino samples.

The Salton Trough, which includes the sampling regions of Coachella Valley and Salton Sea, is ~180 km long and contains a number of complex faults, all of which are part of the SAFS. The northern part of the Salton Trough, the Coachella Valley, is bounded by the Little San Bernardino Mountains in the east and by the San Jacinto Mountains in the west (Goldrath, 2007) (Figure 2.1.2).

Figure 2.1.2: Map of Salton Trough (Coachella Valley and Salton Sea) study area with labeled sample locations. Major mountain ranges, faults, and features also labeled.

These two mountain ranges are primarily Precambrian granites and metamorphic rocks (Jennings, 1967). In the southern part of the Salton Trough, the Imperial Valley, the east trough wall is bordered by the SAFS in contact with the Chocolate and Orocopia Mountains, with Precambrian metamorphics and granites and Mesozoic plutons and schists (Jennings, 1967). The western trough wall is bounded by the Santa Rosa Mountains, consisting of Cretaceous plutonic rocks, the Southern California batholith, and metamorphic host rocks (Wallace, 1990). There is a gap in the crystalline basement, which is filled with Quaternary and older Cenozoic sediments

(Fuis et al, 1984). As found by Fuis et al. (1982) through seismic refraction studies, the basement is 5-6 km deep within the trough. This "basement", however, is thought to be metamorphosed Cenozoic fill. Near the southern end of the Salton Sea, the SAFS terminates into a pull-apart basin, which is the most northerly component of a series of pull-apart basins distributed throughout the Gulf of California that form part of the East Pacific Rise (Wallace, 1990). Although the Salton Trough has experienced large earthquakes in the past (1020, 1300, 1450, and 1680), there have been no significant earthquakes along this section of the SAFS since 1680.

Directly south of the SAFS termination, however, is the Brawley Seismic Zone (BSZ), defined by a dense cluster of earthquake epicenters, connecting to the Imperial Fault in the south (Wallace, 1990; Onderdonk, 2011). There was an earthquake swarm from August 25-27, 2012 centered ~5 km NNW of Brawley, CA within the BSZ. During the swarm, the largest two earthquakes were recorded as M5.3 and M5.5 on August 26, 2012. The 2012 events were the largest earthquakes in the area since 1981, when there was a recorded M5.9 (U.S. Geological Survey, 2013). The BSZ terminates at the northernmost section of the Imperial fault, and delineates the boundary between the North American and Pacific plates (Yeats, 2012). The BSZ is one of two on-land spreading centers that are associated with the Gulf of California and the East Pacific Rise (the other being Cerro Prieto in Baja California). These two spreading centers are onshore because the crust is largely continental and buoyant and they are both covered with deltaic sediments from the Colorado River (Yeats, 2012). High heat flow

characteristic of spreading centers is expressed by the mud volcanoes and rhyolite domes (Obsidian Butte) found on the southern end of the Salton Sea (Yeats, 2012).

The San Bernardino Valley is an area restricted to the upper portion of the Santa Ana Basin between the San Jacinto and San Andreas faults and bounded by the San Gabriel Mountains in the north and the Crafton Hills in the south, as defined by Dutcher and Garrett (1963) (Figure 2.1.3). The surrounding mountain ranges are primarily composed of Precambrian and Tertiary igneous and metamorphic rocks which also comprise the basement of the basin (Morton and Matti, 1993). The basement is overlain by Holocene to Pleistocene riverine deposits and alluvium (Danksin, 2005). There is considerable subparallel faulting within the San Bernardino Basin (Dutcher and Garrett, 1963; Morton and Matti, 1993; Danskin et al., 2005; Woolfenden and Kadhim, 1997) that has split the larger basin into smaller constituent basins. Many of the faults within the sediment basin are abandoned fault traces of the SJF, however. The primary influence of these faults is impedance of groundwater flow (Woolfenden and Kadhim, 1997). This area, however, is tectonically active as indicated by numerous nearby earthquakes, including many above M5.0. In 1992, there were two earthquakes at M7.3 and M6.1 (Roeloffs et al., 1995).
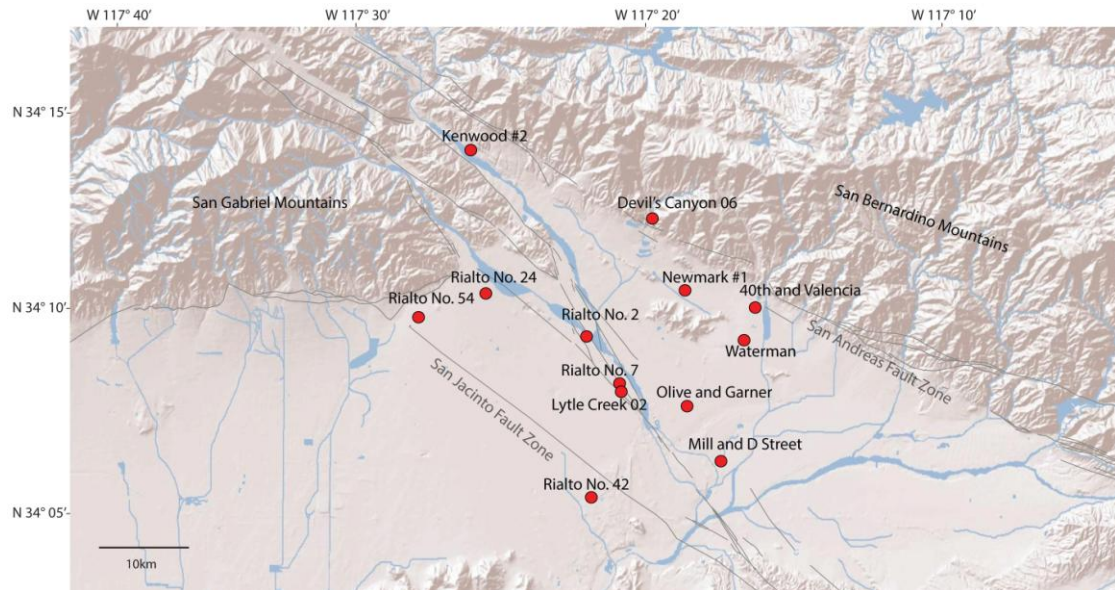
Figure 2.1.3: Map of San Bernardino Basin study area with labeled sample locations. Major mountain ranges and faults labeled.

2.2. Hydrogeologic Setting:

The Salton Trough is primarily composed of silt and fine-grained sand deposited by the Colorado, Whitewater, and San Gorgonio rivers and silts, sands and gravels deposited as alluvium from the adjacent Chocolate, Orocopia and Santa Rosa mountains (Muffler and White, 1969; Goldrath, 2007). Sand and gravel units are inter-layered with silts and clays deposited during lacustrine settings during periodic inundation of the Salton Trough (unpub. Kelliher, 2006). Coarse-grained sediments contribute large storage capacity for groundwater in the area, but are not usually laterally continuous throughout the basin (Muffler and White, 1969). In 1942, the All American Canal was completed to supply high quality Colorado River water to the southern Imperial Valley, and in 1949, the 196 km Coachella Canal, consisting of both lined and unlined sections, was added to provide the same Colorado River water to the northern portion of the Salton Trough (Nadeau, 1997).

There are two distinct aquifer units within the Salton Trough. First, there is a shallow, unconfined aquifer (ranging in thickness from 1 to 75 meters) contained in the basin fill underlain by a 1 to 75 meter thick aquitard. Second, there is a deeper, semi-confined basin fill aquifer (ranging in thickness from 3 to 180 meters) which is bound above by the same aquitard and below by the impermeable "basement" rock, or metamorphosed Cenezoic fill (unpub. Kelliher, 2006). The groundwater flow of the area is generally south to southwest; however, the SAFS acts as an impermeable boundary throughout much of the fault trace, especially in the Coachella Valley (Proctor, 1968). There are several sources of groundwater recharge to the Salton Trough including (1) precipitation in the trough (roughly 100-120 cm/year), (2) stream- and river-flow infiltration from runoff from the surrounding mountains, (3) Colorado River water seepage via the Coachella Canal, and (4) percolation from irrigation throughout the Coachella and Imperial valleys (Goldrath, 2007).

The San Bernardino Basin is filled with ~300 m to >1000 m of Holocene river-channel deposits and Holocene and Pleistocene alluvium consisting of gravels, sands, and silts (Danskin et al., 2005; Woolfenden and Kadhim, 1997). The loosely consolidated material of the basin serves as permeable storage for groundwater in the area. However, much of the groundwater flow is impeded by the numerous fault traces, so many of the aquifer units are laterally separated. The surficial water-bearing units are unconfined to partly-confined, excluding the underlying consolidated silts and clays, which are not part of the groundwater system (Woolfenden and Kadhim, 1997). Recharge of the unconfined aquifer in the area is subject to two primary water

sources: (1) seepage/runoff from the San Gabriel and San Bernardino mountains in the forms of Lytle Creek and Santa Ana river, and (2) infiltration of 40-80 cm of precipitation per year (Woolfenden and Kadhim, 1997: Danskin et al, 2005).

3. Sampling and Analytical Methods

3.1. Site selection

A set of sample sites was selected using a Quaternary Fault Map available through the US Geological Survey's website (US Geological Survey, 2013) along with a database of wells acquired through the USGS (pers comm., Justin Kulongoski, USGS). Wells that are located within a few kilometers of the SAFS (or either the SAFS or SJFZ in the San Bernardino Basin) were selected for sampling.

There were six separate field trips to collect the water samples used in this study. The trips took place over the period of January, 2011 to August, 2012. The first two trips were to the Coachella Valley to collect groundwater samples along the SAF. The third trip was to the eastern shore of the Salton Sea and the samples were collected from both hydrothermal spring wells and groundwater wells. The subsequent two trips were to the San Bernardino area to collect groundwater well samples. The samples were attained from the San Bernardino Water District in the fourth trip and from West Valley Water District in the fifth. Immediately following an earthquake swarm centered near Brawley, CA (approximately 40 km south of the Salton Sea sample area), the same six localities in the Salton Sea area (trip 3) were resampled.

3.2. Groundwater Sampling for Dissolved Gases

Prior to sampling, all wells were required to be pumped until approximately three times the well casing volume had been extracted. To collect the helium and

carbon gas dissolved in the groundwater and hot spring samples, $^1/_4$" and $^3/_8$" annealed copper tubes were used. The use of copper preserves the integrity of the sample even after extended periods of storage due to the low permeability of copper to helium (Weiss 1968). A sampling apparatus was assembled, connecting the copper tubes to the wellhead using Tygon™ tubing. Once all of the air bubbles had been pushed through the tubing, the copper tubes were sealed. On the downstream end of the tubes, a refrigeration clamp was used to seal the tube, and the other side was sealed using a cold weld crimper (Kulongoski and Hilton, 2011). Two $^1/_4$" tubes and one $^3/_8$" copper tube were collected at each site.

3.3. Groundwater sampling for Chemistry

At each sample site, a total of four 125 mL bottles were filled with sample water. Two of the 125 mL bottles had been previously poisoned with 5 µL of HgCl in preparation for later alkalinity measurements (Dickson et al, 2003), and then filled with groundwater at the site. The other two 125 mL bottles were rinsed three times with groundwater and then filled leaving a small headspace volume. The samples were *not* acidified immediately after sampling because the anion and the cation chemistry were analyzed using the same bottle (Clark and Fritz, 1997). The temperature of the water was recorded at each site. The pH and total dissolved solids (mg/L) were recorded within the week after sampling using an Oakton Multi-Parameter PTTestr™ 35 at the Fluids and Volatiles Laboratory at Scripps Institution of Oceanography.

The major ion chemistry data of the groundwaters from Coachella Valley was acquired through the U.S. Geological Survey (pers comm., Kulongoski, USGS).

3.4. Laboratory analysis

The samples were processed using an ultra-high vacuum extraction line in the Fluids and Volatiles Laboratory at Scripps Institution of Oceanography (Kulongoski and Hilton, 2002). The samples were weighed before and after the extraction to determine the amount of water in the sample. First, the water sample in the $^1/_4$" copper tube was connected to the extraction line using standard high vacuum fittings. The water was released into a degassing bulb where it reacted with phosphorus pentoxide to ensure that all of the CO_2 (dissolved and in the form of HCO_3^-/CO_3^{2-}) was released from the water phase. Water vapor was isolated from the sample using a water-trap held at -78 °C (cooled using a slurry of acetone and dry ice). Subsequently, the CO_2 was frozen onto a stainless steel U-tube cooled by liquid nitrogen. Finally, the He and Ne were isolated using a Ti-getter heated to 700 °C (to remove N_2, CO, and CH_4) and a charcoal finger at liquid nitrogen temperature (to remove Ar, Kr, and Xe).

On the extraction line, a known split of the He-Ne portion (~0.4%) of the exsolved gas was equilibrated with a $^1/_4$" copper tube finger which was sealed with a cold weld crimper for transfer to a MAP-215 noble gas spectrometer for further purification and analysis (Kulongoski and Hilton, 2011). The helium and neon gases were inlet in to the mass spectrometer sequentially and sample peak intensities were compared with prepared standards of atmospheric air (Kulongoski et al., 2003). Errors

of the helium and neon contents contain uncertainties associated with reproducibility

of duplicate analysis (usually good to $\pm 2\%$). The CO_2 portion of the sample was

condensed into a $^1/_4$" copper tube finger from the extraction line and then sealed and

transferred to a separate purification line for manometric measurement of the total

amount of gas. Then the CO_2 was re-sealed into a Pyrex glass finger for transfer and

analysis for isotopic composition using a Thermo Finnigan Delta XP$_{PLUS}$ stable

isotope mass spectrometer (see description by Barry et al, 2013). The international

Vienna Pee Dee Belemnite (VPDB) standard was used for calibration with a precision

of less than 0.1‰. The accuracy of the $\delta^{13}C$ determinations (± 0.5‰) is estimated by

repeat analysis of a working laboratory standard, itself calibrated relative to VPDB

(Barry et al, 2012).

The concentrations of major cations (Ca^+, Mg^+, Na^+ and K^+) were determined

using a PerkinElmer® Optima 3000DV inductively coupled plasma optical emission

mass spectrometer (ICP-OES) at Scripps Institution of Oceanography. Sample

preparation and instrument procedure is similar to that described in Janney and

Castillo (1996). The water samples were centrifuged and then 50 μL of clear aliquots

were diluted up to 5 mL with a 1% HCl solution made from doubly-distilled water and

reagent. Calibration curves at the beginning of each analytical run were constructed

using PerkinElmer® Pure *Plus* Atomic Spectroscopy Standard. Detection limits for

each element are based on a 98% confidence level (3 standard deviations). A

correlation coefficient of greater than 0.9990 was accepted for each separate analyte.

Accuracy and precision were monitored by repeated analyses of an international water

standard, the Riverine Water SLRS-3 from the Institute of Environmental Chemistry, National Research Council Canada. There was no substantial instrumental drift detected during the analysis as indicated by the reproducibility of the standard throughout each run. All of the analytes of the samples had less than a 6% RSD error.

Concentrations of major anions (F^-, Cl^-, NO_3^-, and SO_4^{2-}) were determined using an Ion Chromatograph (Metrohm 850 Professional Ion Chromatograph) at the California Water Science Center at US Geological Survey in San Diego, CA following the guidelines of the EPA Method 300.1 (Hautman and Munch, 1997). Prior to analysis, 10 mL of the water samples were filtered using 0.45 µL PES syringe filters. Then the samples underwent analysis by the Ion Chromatograph. The samples passed through a 0.2 µm filter and then a column of tightly packed polymer beads, each coated with numerous positively-charged quaternary-ammonium functional groups. Cations pass through the system quickly; however, anions have an affinity for the positively charged coating. The degree to which each anion is retained depends on the type of charge and distribution across the ion, and is the basis for separation by this method. The system is calibrated with seven working standards and a reagent blank. A calibration curve is prepared by plotting peak area versus known concentration for all the working standards and reagent blank. The correlation coefficient of the regression analysis has to be 0.995 or greater to be considered acceptable. Because nonlinear responses can result when the column capacity for an analyte is exceeded, the sample concentrations must fall within the calibration range for each analyte. Samples with

high concentrations of a certain analyte must be diluted accordingly so as to ensure reproducibility (Methods of Analysis by USGS, 2008).

Alkalinity was measured by the laboratory staff employed by Prof. Andrew Dickson at Scripps Institution of Oceanography. The total alkalinity was estimated using a two-state potentiometric titration kept at a constant temperature of ~20 °C using HCl (Dickson et al, 2003). The sample was acidified to a pH between 3.5 and 4.0. The titration was then continued to a pH of ~3.0. Using a least-squares procedure that calculates the total alkalinity, the equivalence point was evaluated. For quality control, standards of seawater and house tap water were run as a part of the sample analysis. The standard deviation of the standards was ~5 µmol/kg and the repeatability typically at <1%. The overall uncertainty for the unknown samples with alkalinities greater than 500 µmol/kg was about 1%, and for samples with alkalinities less than 500 µmol/kg was a little larger than 1%.

4. Results

The helium and CO_2 results (isotopic compositions and concentrations) are shown in Table 1. The major ion water chemistry, including alkalinity and saturation index, are shown in Table 2.

4.1. Helium-4 Concentrations

In Table 1, the measured helium concentrations (cm^3 STP/g H_2O) are given and have been corrected for air-derived helium from air equilibration using measured $^4He/^{20}Ne$ measurements and the following equations:

$$X = \frac{\left(\frac{^4He}{^{20}Ne}\right)_m}{\left(\frac{^4He}{^{20}Ne}\right)_{air}} \times \frac{\beta Ne}{\beta He}$$

$$[\,^4He]_C = \frac{[\,^4He]_M \times (X-1)}{X}$$

where $(^4He/^{20}Ne)_m$ is the measured ratio, $(^4He/^{20}Ne)_{air}$ is the ratio of air, and β is the Bunsen solubility coefficient calculated for Ne and He (= 1.23 @ 20°C – average temperature of recharge; Weiss, 1971; Torgerson, 1980; Kulongoski, 2008).

Groundwaters in the Salton Sea and Coachella Valley, i.e. Salton Trough, have higher He concentrations (median $[\,^4He]_C = 46.3$ x 10^{-8} cm^3 STP/g H_2O) than the San Bernardino area (median $[\,^4He]_C = 7.1$ x 10^{-8} cm^3 STP/g H_2O). Almost all of the

Table 1: Helium and carbon data.

Well ID[a]	Latitude °N	Longitude °W	Distance to Any Fault km	Elevation m	R_M/R_A[b]	X[c]	R_C/R_A[d] ±1σ	Percent mantle[e] %	$[^4He]_M$[f]	$[^4He]_C$[f]	$[CO_2]$[g]	δ13C[h] ‰ VPDB	$CO_2/^3He$ x 10^{10}
San Bernardino													
Olive and Garner	34.1186	-117.3118	2.2	342	1.12	1.30	1.52±0.24	18.8	1.80	0.41	7.97	-11.78	124
Lytle Creek 02	34.1260	-117.3488	0.1	376	1.16	1.90	1.35±0.24	16.7	1.25	0.59	5.08	-16.81	52.9
Newmark #1	34.1732	-117.3130	1.7	426	1.30	1.72	1.72±0.30	21.3	1.15	0.48	7.35	-13.98	84.3
Devils Canyon 06	34.2070	-117.3319	0.3	613	1.04	2.24	1.07±0.12	13.2	0.58	0.32	9.33	-12.57	200
Kenwood #2	34.2388	-117.4348	0.3	711	0.57	3.52	0.40±0.05	4.80	2.41	1.73	10.81	-16.34	78.1
40th and Valencia	34.1652	-117.2733	0.6	403	0.91	2.01	0.83±0.07	10.2	0.63	0.32	7.34	-13.33	182
Waterman Well	34.1485	-117.2796	2.1	378	0.96	2.57	0.94±0.04	11.5	2.20	1.34	9.18	-13.01	50.7
Rialto No. 24	34.1719	-117.4265	0.6	567	1.35	2.92	1.53±0.25	18.9	1.27	0.83	5.87	-15.21	37.3
Rialto No. 54	34.1616	-117.4663	0.7	513	0.96	1.86	0.92±0.07	11.3	30.4	14.1	5.89	-16.31	3.10
Rialto No. 2	34.1515	-117.3691	0.1	430	1.21	1.40	1.73±0.18	21.4	3.94	1.13	4.86	-15.78	25.4
Rialto No. 7	34.1302	-117.3508	0.0	380	1.18	1.83	1.39±0.18	17.2	2.78	1.26	6.45	-13.92	31.1
Rialto No. 42	34.0759	-117.3663	4.7	325	1.39	2.20	1.71±0.29	21.2	0.97	0.53	6.96	-14.64	67.7
Coachella Valley													
Eisenhower MC1	33.7641	-116.4072	9.1	n.d.	0.92	4.88	0.91±0.09	11.0	3.31	2.63	6.16	-11.50	18.6
WCAS Dillon #1	33.7863	-116.1796	4.1	132	0.19	91.9	0.18±0.01	2.00	55.1	55	3.10	-9.20	2.88
Grant Street Farm	33.5509	-116.0408	5.6	n.d.	0.72	4.57	0.64±0.06	7.80	3.99	3.12	5.30	-4.60	19.0
Grant Street Farm-(R)	33.5509	-116.0408	5.6	n.d.	0.73	5.11	0.66±0.06	8.00	4.07	3.27	5.25	-4.70	17.4
MSWD 27	33.9245	-116.5406	0.6	n.d.	0.95	3.88	0.93±0.06	11.4	2.76	2.05	5.86	-12.10	21.9
MSWD 27-(R)	33.9245	-116.5406	0.6	n.d.	0.88	4.51	0.85±0.07	10.4	2.62	2.04	5.44	-12.80	22.4
MSWD 29	33.9509	-116.5184	1.8	n.d.	0.71	3.25	0.58±0.02	7.00	7.86	3.77	6.20	-10.36	20.4
MSWD 31	33.9241	-116.5403	0.6	261	0.63	7.39	0.57±0.01	6.90	10.7	8	4.27	-13.83	6.70
MSWD 24	33.9603	-116.5251	1.5	261	0.92	1.95	0.83±0.02	10.2	6.47	1.53	7.84	-10.50	43.8
CVWD 6807-1	33.6135	-116.1076	4.5	-45	0.62	3.79	0.48±0.01	5.80	6.70	3.63	2.62	-11.35	10.7
CVWD 6805	33.6386	-116.1912	8.5	-32	0.62	4.34	0.50±0.01	6.00	7.05	4.18	2.94	-12.44	10.0
CVWD 4722	33.7831	-116.3931	6.7	-32	0.80	2.26	0.64±0.01	7.80	3.96	1.23	3.40	-11.03	30.8
CVWD 4630	33.8199	-116.3931	3.1	n.d.	0.73	2.59	0.56±0.01	6.80	3.17	1.73	n.a.	n.a.	n.a.
CVWD 4563	33.8483	-116.4755	4.5	135	0.99	1.81	0.97±0.02	11.9	3.91	1.21	1.78	-11.00	10.8
WCAS Airport	33.6422	-116.0861	0.9	17	0.25	13.8	0.19±0.003	2.10	16.9	10.8	2.20	-10.24	7.60
Salton Sea													
Pacific Aquafarms	33.4230	-115.6793	0.2	-16	1.16	44.5	1.17±0.09	14.4	6.82	6.67	27.0	-8.67	24.8
Pacific Aquafarms - 2	33.4230	-115.6793	0.2	-16	1.11	24.1	1.12±0.10	13.8	3.55	3.4	21.2	-7.84	39.9
Bashfords	33.4230	-115.6818	0.5	-20	1.18	22.6	1.19±0.10	14.7	6.57	6.28	19.9	-8.23	19.0
Bashfords - 2	33.4230	-115.6818	0.5	-20	1.20	32.4	1.21±0.09	14.9	4.78	4.63	15.9	-7.96	20.4
Fountain of Youth	33.4001	-115.6601	0.5	-6.0	2.09	48.4	2.11±0.16	26.2	10.1	9.86	38.4	-8.22	13.3
Fountain of Youth - 2	33.4001	-115.6601	0.5	-6.0	1.96	38.2	1.99±0.17	24.7	9.45	9.21	36.5	-7.67	14.4
Well T7A	33.5089	-115.8255	6.0	-23	0.65	6.36	0.58±0.06	7.00	1.40	1.18	6.88	-6.35	64.6
Well T7A - 2	33.5089	-115.8255	6.0	-23	0.97	2.69	0.95±0.05	11.7	36.2	22.7	9.42	-7.97	3.06
Well T5	33.5068	-115.8179	6.4	-21	1.62	2.02	2.23±0.36	27.7	0.97	0.49	17.0	-10.04	153
Cox Oasis	33.5038	-115.8383	5.0	-21	1.00	5.45	1.00±0.11	12.3	2.33	1.9	6.62	-10.65	24.9
Cox Oasis - 2	33.5038	-115.8383	5.0	-21	1.13	7.63	1.15±0.12	14.2	1.81	1.57	7.14	-8.11	28.8

[a]Samples labeled with (R) are duplicates, samples with -2 are localities resampled following August 26th, 2012 earthquake.

[b]R_M/R_A is measured $^3He/^4He$ ratio divided by the $^3He/^4He$ in air=1.4×10^{-6}.

[c]X-value is $(^4He/^{20}Ne)_{measured}/(^4He/^{20}Ne)_{air}\times(\beta Ne/\beta He)]$, where β = Bunsen solubility coefficient. For pure water at 15 °C $(\beta Ne/\beta He)=1.22$ (Weiss, 1971).

[d]R_C/R_A is the air corrected He isotope ratio=$[(R_M/R_A\times X)-1]/(X-1)$.

[e]Calculated using simple binary mixing model between $8R_A$ (mantle He) and $0.02 R_A$ (crustal He).

[f]10^{-7} cm^3 STP/gH$_2$O

[g]10^{-2} cm^3 STP/gH$_2$O

[h]Accuracy is ± 5‰.

samples in the Salton Trough have higher helium concentrations than air-saturated

water (ASW) (4.48 x 10^{-8} cm^3 STP/g H$_2$O; Weiss, 1971). Most samples from San

Bernardino show helium concentrations very close to ASW values (Weiss, 1971).

4.2. ^{3}He/^{4}He ratios

　　The measured ^{3}He/^{4}He ratios (Table 1) have been corrected for air-equilibrated

helium using the following equation:

$$\frac{R_C}{R_A} = \frac{\frac{R_M}{R_A} \times (X-1)}{(X-1)}$$

where R_C/R_A is the air corrected ^{3}He/^{4}He ratio (R_C) normalized to ^{3}He/^{4}He ratio of air

(R_A = 1.4 x 10^{-6}; Clarke et al. 1976) and X is defined above. Samples in the Coachella

Valley all present corrected ^{3}He/^{4}He ratios less than 1 R_A (0.19 – 0.97 R_A), which are

much less variable than the San Bernardino and Salton Sea samples. Salton Sea

groundwaters contain ^{3}He/^{4}He ratios from 0.58-2.23 R_A and San Bernardino wells

have ^{3}He/^{4}He ratios from 0.40-1.73 R_A (Table 1).

　　This procedure allows a simple determination of the relative proportion of

mantle- (8 R_A; Graham, 2002) and crustal-derived (0.02 R_A; Andrews, 1985) He in

each sample. Percent mantle contribution was calculated using a simple binary mixing

model using 8 R_A as the mantle endmember and 0.02 R_A as the crustal endmember to

stay consistent with the previous studies of Kennedy et al (1997) and Kulongoski et al.

(2013), noting, however, that 6 R_A may be a more appropriate choice for subcontinental mantle (Dunai and Baur, 1995; Dunai and Porcelli, 2002).

The median percent mantle contribution in the Salton Sea and San Bernardino samples are 14.4% and 16.9%, respectively. Meanwhile, Coachella Valley shows a significantly lower mantle contribution with a median value of 7.8%.

4.3. $CO_2/^3He$

The $CO_2/^3He$ ratios in the samples range from 0.091 to 200 (x 10^{10}) (Table 1). San Bernardino has the largest median $CO_2/^3He$ ratio at 60.3 (x 10^{10}), while Coachella Valley and Salton Sea are 18.0 (x 10^{10}) and 24.80 (x 10^{10}), respectively. Almost all of these values display values between mantle- (2 ± 1 x 10^9; Marty and Jambon, 1987) and crustal-derived components (10^{11} to 10^{14}) (O'Nions and Oxburgh, 1988), but are much more weighted towards crustal values.

4.4. CO_2 concentrations and carbon isotopes

Concentrations of CO_2 in the groundwaters vary from 2.62 to 38.4 (x 10^{-2} cm^3 STP/g H_2O) (Table 1). Salton Sea groundwaters have the highest median concentration of CO_2 (16.9 x 10^{-2} cm^3 STP/g H_2O). San Bernardino and Coachella Valley groundwaters have median CO_2 concentrations of 7.2 (x 10^{-2} cm^3 STP/g H_2O) and 4.8 (x 10^{-2} cm^3 STP/g H_2O), respectively.

Most of the groundwater samples (Table 1) have $\delta^{13}C$ (CO_2) values lower than typical mantle values (-6.5 $\pm$ 2‰; Pineau and Javoy, 1983; Sano and Marty, 1995).

San Bernardino, Coachella Valley, and Salton Sea have median $\delta^{13}C$ values of -14.31‰ (range of -11.78 to -16.81‰), -11.02‰ (range of -4.60 to -13.83‰), and -8.11‰ (range of -6.35 to -10.65‰), respectively.

4.5 Major ion chemistry

The major ion chemistry of the groundwaters is reported in Table 2. The Salton Sea groundwaters contain the highest total dissolved solids (TDS) with a median of 3360 mg/L, while San Bernardino is much lower with a median of 290 mg/L. Coachella Valley groundwaters have a median specific conductance of 740 μS. The reason that the Salton Sea has much higher TDS is that the waters contain very high Cl^- and Na^+ concentrations (median = 1540 and 1034 mg/L, respectively). However, groundwaters of the Coachella Valley and San Bernardino are almost exclusively sulfate waters (see Table 2 for description of water type determination) while Salton Sea represents a mixture of sulfate and chloride groundwater types (Figure 4.5.1). In addition, Salton Sea groundwaters have a higher alkalinity (as $CaCO_3$) (average = 224 mg/L) than Coachella Valley (average = 128 mg/L) and San Bernardino (average = 145 mg/L). However, the saturation indices (calcite) of the groundwaters are all roughly similar with Salton Sea, Coachella Valley, and San Bernardino at -0.217 ± 0.668, 0.168 ± 0.207, and -0.570 ± 1.33, respectively. A supersaturated solution (with respect to calcite) is denoted by a positive saturation index and an undersaturated solution is denoted by a negative saturation index (Hiscock, 2005).

In addition, the temperature of Salton Sea groundwaters are much higher (average = 49.2ºC) than San Bernardino and Coachella Valley groundwaters that have average temperatures of 18.1ºC and 26.5ºC, respectively.

Table 2: Water Chemistry.

| Location	T (°C)	pH	Water type	TDS ppm	Alkalinity[c] mg/kg	F mg/L	Cl mg/L	NO3 mg/L	SO4 mg/L	Ca mg/L	Na mg/L	Mg mg/L	K mg/L	Charge Balance[d]	S.I.[e]
San Bernardino															
Olive and Garner Street Well	21.4	7.5	CaSO4	324	171.5	0.60	8.5	1.80	52	57.92	18.53	13.85	4.65	3.57	0.01
Lytle Creek 02	20.3	7.8	CaSO4	210	132.4	0.28	4.6	1.40	26	39.48	21.04	2.89	2.63	2.48	0.05
Newmark #1	20.2	7.3	CaSO4	325	135.4	0.25	49	1.40	42	52.29	27.20	10.45	3.36	2.44	-0.35
Devil's Canyon 06	4.30	7.0	CaSO4	290	164.9	0.25	23	0.67	33	52.91	20.47	12.38	3.54	3.28	-3.37
Kenwood #2	18.1	7.3	CaSO4	390	188.3	0.91	15	2	86	73.40	28.25	17.46	4.29	4.14	-0.11
40th and Valencia	18.5	6.9	Na2SO4	377	114.7	1.10	48	1.60	102	44.14	52.71	10.74	4.13	1.92	-0.91
Waterman Well	19.1	7.3	CaSO4	369	151.2	0.35	51	3.20	51	67.26	16.15	12.97	3.53	2.65	-0.22
Rialto No. 24	16.6	7.7	CaSO4	214	146.4	0.19	7.9	4.90	25	48.80	8.99	7.73	2.87	2.70	0.02
Rialto No. 54	21.3	8.0	CaSO4	261	157.9	0.24	4.1	2.10	20	47.89	16.11	7.61	2.15	3.19	0.40
Rialto No. 2	18.0	7.9	CaSO4	209	127.2	0.28	4.2	2.30	21	43.86	13.50	3.90	2.41	2.55	-3.24
Rialto No. 7	19.9	8.0	CaSO4	274	137.9	0.14	6.4	1.20	31	47.26	14.04	4.38	2.81	2.55	0.33
Rialto No. 42	19.9	8.1	CaSO4	226	157.9	0.33	3.4	0.90	27	56.24	15.05	5.79	2.67	3.31	0.55
Salton Sea															
Pacific Aquafarms	72.0	6.5	NaCl	3360	260.9	4.40	1590	0	225	144.3	1066	23.78	63.98	7.38	-1.67
Pacific Aquafarms - 2	58.0	7.3	KCl	3540		3.50	1607	0	205	151.5	1148	25.40	66.00	11.46	
Bashford's Mineral Spa	66.9	6.4	NaCl	3410	237.4	5.90	1540	0	236	150.5	1034	22.65	60.04	7.21	-0.27
Bashford's Mineral Spa Resample - 2	71.2	7.4	KCl	3610		4.70	1609	0	208	158.1	1137	24.30	63.50	10.98	
Fountain of Youth Campground	66.3	6.5	NaCl	4030	371.9	3.90	1840	0	217	176.6	1242	30.85	69.51	10.52	0.06
Fountain of Youth Campground Resample - 2	53.6	7.2	KCl	4550		3.30	2040	0	215	181.9	1454	33.70	82.40	14.98	
Well T7A at Dos Palmas	37.5	7.5	Na2SO4	1040	157.7	1.00	237	1.10	333	72.47	208.3	32.10	14.29	1.99	0.20
Well T7A at Dos Palmas Resample - 2	29.2	8.0	K2SO4	926		0.72	189	0	299	67.00	190.4	31.00	11.50	2.87	
Well T5 at Dos Palmas	28.7	8.1	K2SO4	826	152.2	1.20	136	0	290	50.20	173.7	24.60	10.70	2.41	0.23
Cox Oasis at Dos Palmas	27.9	7.9	Na2SO4	997	166.9	2.80	195	0.67	349	30.97	272.6	14.30	12.29	1.96	0.15
Cox Oasis at Dos Palmas Resample - 2	29.6	8.3	K2SO4	1060		1.90	196	0	327	32.50	286.2	15.90	10.60	3.20	
Coachella Valley[a]				Spec. Cond[b]											
Eisenhower MC1	21.1	7.9	CaCO3	409	162	0.53	13	0	35.5	50.2	20.5	8.7	3.69	3.07	0.31
WCAS Dillon	34.9	8.1	Na2SO4	1330	106	3.21	88.9	0	385	31.7	224	6.28	8.36	1.35	0.12
Grant St Farm	26.2	8.5	Na2SO4	746	44	6.99	50.5	0	174	15.6	155	1.14	1.63	2.24	-0.19
Grant Street Farm-(R)	25.0	n.d.	n.d.	n.d.	n.d.	n.d.	n.d.	n.d.	n.d.	n.d.	n.d.	n.d.	n.d.	n.d.	n.d.
MSWD 27	26.5	7.8	Na2SO4	478	120	0.57	29.5	0	69	38.3	49.5	5.77	7.09	2.42	0.02
MSWD 27-(R)	n.d.	n.d.	n.d.	n.d.	n.d.	n.d.	n.d.	n.d.	n.d.	n.d.	n.d.	n.d.	n.d.	n.d.	n.d.
MSWD 29	29.0	7.9	Na2SO4	735	176	0.78	19.6	0	199	48.2	78.6	13.4	7.73	2.38	0.33
MSWD 31	28.1	n.d.	n.d.	n.d.	n.d.	n.d.	n.d.	n.d.	n.d.	n.d.	n.d.	n.d.	n.d.	n.d.	n.d.
MSWD 24	25.6	n.d.	n.d.	n.d.	n.d.	n.d.	n.d.	n.d.	n.d.	n.d.	n.d.	n.d.	n.d.	n.d.	n.d.
CVWD 6807-1	27.0	n.d.	n.d.	n.d.	n.d.	n.d.	n.d.	n.d.	n.d.	n.d.	n.d.	n.d.	n.d.	n.d.	n.d.
CVWD 6805	23.3	n.d.	n.d.	n.d.	n.d.	n.d.	n.d.	n.d.	n.d.	n.d.	n.d.	n.d.	n.d.	n.d.	n.d.
CVWD 4722	25.3	n.d.	n.d.	n.d.	n.d.	n.d.	n.d.	n.d.	n.d.	n.d.	n.d.	n.d.	n.d.	n.d.	n.d.
CVWD 4630	24.4	n.d.	n.d.	n.d.	n.d.	n.d.	n.d.	n.d.	n.d.	n.d.	n.d.	n.d.	n.d.	n.d.	n.d.
CVWD 4563	20.9	n.d.	n.d.	n.d.	n.d.	n.d.	n.d.	n.d.	n.d.	n.d.	n.d.	n.d.	n.d.	n.d.	n.d.
WCAS Airport Well	33.0	8.0	Na2SO4	1490	158	1.03	212	0	287	53.5	239	5.41	4.61	1.61	0.41

[a]Data acquired from USGS

[b]μS

[c]as CaCO3

[d]calculated using meq/L for each analyte

[e]saturation index as calcite

n.d. = not determined
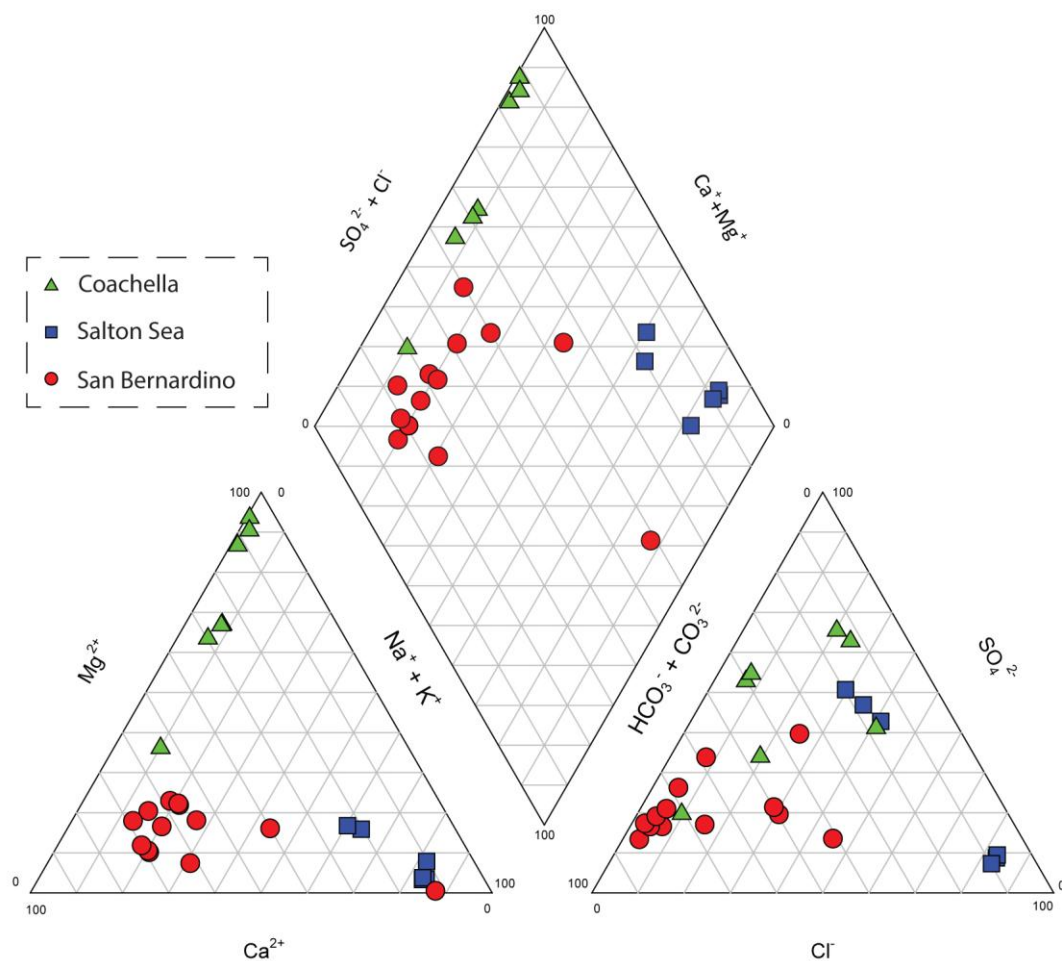
Figure 4.5.1: Piper plot of groundwaters in San Bernardino Basin, Salton Trough, and Coachella Valley. Coachella Valley water chemistry provided by USGS, San Diego (pers. comm., Kulongoski, USGS). Analyses are plotted on basis of the percent of each cation (left ternary plot) or anion (right ternary plot). The cation and anion point of a single sample is projected onto the diamond-shaped field and the intersection of the two lines is where the sample point lies on the diamond plot (Fetter, 1980).

5. Discussion

The following sections discuss helium and carbon provenance and distribution in groundwater samples taken from the Salton Sea, Coachella Valley, and San Bernardino areas, all situated along or immediately adjacent to the SAFS and SJFZ. Furthermore, flux estimates of helium and carbon along the various segments of the faults are calculated and compared.

5.1. Origin of high $^3He/^4He$ ratios in southern California

Previous helium studies along the San Andreas Fault suggest that wells close to the fault record higher mantle-derived helium contributions than wells situated more distally (Kennedy et al., 1997; Kulongoski et al., 2013). Kennedy et al. (1997) note a modest trend of higher $^3He/^4He$ ratios (~0.5-2.1 R_A) near the SAFS (0-20 km) and lower $^3He/^4He$ ratios (~0.2-1.0 R_A) farther away (20-80 km from SAFS), save a single locality that displayed a ~50% (4 R_A) mantle contribution about 30 km from the SAFS. Kulongoski et al. (2013) recorded higher $^3He/^4He$ ratios (0.10-3.52 R_A) near the fault in the Big Bend region (0-10 km from SAFS) with significantly lower $^3He/^4He$ values (0.20 to 1.00 R_A) farther away (10-25 km from SAFS). Both studies argued that helium-rich fluids use the SAFS as a pathway to the surface. This study also shows the same trends with $^3He/^4He$ ratios as high as 2.23 R_A measured within 6.2 km of the SAFS in the Salton Sea region (Fig. 5.2.1).

Helium isotope ratios significantly higher than radiogenic (crustal) production values can result from the transport of helium and helium-rich fluids from the upper mantle melts through the SAFS and SJFZ to the shallow crust (Kennedy et al., 1997; Kulongoski et al., 2003, 2005). According to the 1-dimension model developed by Kennedy et al. (1997), mantle-helium (8 R_A) is transferred through the whole crust via fault pathways and is diluted en route with crustal (i.e., radiogenic helium produced via ^{238}U, ^{235}U and ^{232}Th decay) helium (0.02 R_A). Higher transfer rates equate to higher $^3He/^4He$ ratios at the surface, as insufficient time is available for steady-state addition of radiogenic helium. Conversely, if transfer of fluids is relatively slow, resultant $^3He/^4He$ ratios will more closely resemble crustal helium because there is sufficient time for the radiogenic helium to dilute the mantle-helium signal (Kennedy et al., 1997).

The Salton Sea groundwater samples contain the highest $^3He/^4He$ ratios of this study, which could be attributed to quick transfer rates of mantle fluids described by Kennedy et al. (1997), but is more likely related to magmatic intrusion at a depth of 10-15 km found below the Brawley Seismic Zone (Fuis et al., 1982; Wallace, 1990). The Brawley Seismic Zone is ~20-30 km south of the sampling region and has frequent earthquake swarm events, which can help facilitate transfer of helium-rich fluids upward via the numerous fault pathways found in the area (Wallace, 1990; Torgerson and O'Donnell, 1991; Kennedy et al., 1997; Woolfenden and Kadhim, 1997). The southern portion of the Salton Sea sits atop the northern-most expression of the East Pacific Rise (EPR), which promotes thinning of the crust which, in turn,

promotes upward flow of partially melted mantle lithosphere (Fuis et al., 1982; Wallace, 1990; Yeats, 2012). This upward flowing magma also contributes mantle-helium, which is manifested in elevated ^{3}He/^{4}He ratios.

The contribution of mantle-helium in Coachella Valley groundwater is considerably less than in Salton Sea groundwater. This is because the magmatic influence seen south of the Salton Sea does not reach as far north as the Coachella Valley area (~65 km to the north). Furthermore, as the SAFS bends just north of San Bernardino, the Coachella Valley undergoes aseismic compression and thickening of underlying crust (Wallace, 1990; Yeats, 2012). With a thicker crust, the mantle-helium has to travel a greater distance to reach the surface, and there is greater potential for dilution by crustal helium (Kennedy et al., 1997).

In the case of San Bernardino, ^{3}He/^{4}He ratios mainly fall above 1 R_A. The SJFZ and SAFS converge in San Bernardino, and with this convergence, there are more fault pathways for mantle fluids to traverse (Wallace, 1990; Woolfenden and Kadhim; 1997; Danskin, 2005). Thus, mantle-helium can potentially be transferred to the surface more quickly through greater permeability of the crust, and this is seen by the slightly elevated ^{3}He/^{4}He ratios compared to the Coachella Valley.

5.2. Spatial variations in ^{3}He/^{4}He ratios

Kennedy et al. (1997) and Kulongoski et al. (2013) noted that within a small distance of the SAFS there is a large variability seen in ^{3}He/^{4}He ratios, ranging from ~0.5 to 2.1 R_A within 10 km of the SAFS in the study by Kennedy et al. (1997) and

0.10 to 3.52 R_A within 1 km of the SAFS in the study by Kulongoski et al. (2013). In the study by Kulongoski et al. (2013), it was determined that within 10 km of the fault, there is a large spatial variability of ^{3}He/^{4}He ratios. However, once one travels beyond the closest 10 km, ^{3}He/^{4}He ratios are indirectly proportional to distance to the fault. So, outside of the 20 km fault zone, ^{3}He/^{4}He ratios fall as one travels farther from the fault trace.

In this study, all wells sampled lie within 10 km of the SAFS or SJFZ. As seen in Figure 5.2.1, there is no clear fault proximity trend in any of the three regions of this study. The highest mantle-helium involvement is found in Salton Sea groundwaters at Well T5 with 27.7% (2.23 R_A). This well is 6 km away from the SAFS. Furthermore, Well T7A is only 580 m from Well T5 and it has a 7.0% (0.58 R_A) mantle-helium contribution. In the Coachella Valley, the well with the highest mantle contribution of 11.9% (0.97 R_A) is CVWD 4563 (4.5 km from the SAFS) while WCAS Airport is only 0.9km away from the fault and shows a mantle contribution of 2.1% (0.19 R_A). Finally, in the San Bernardino study area, mantle involvement varies from 4.8% to 21.4% (0.40-1.73 R_A) with all wells being located less than 4.7 km from either the SJFZ or SAFS. So, within 10 km of a fault in all sampling areas, there is significant variation in mantle involvement in the groundwaters.

There are a number of possible explanations for the heterogeneity in ^{3}He/^{4}He ratios over short distances. First, addition of ^{3}He by decay of bomb tritium in the groundwater could contribute to the observed variations in ^{3}He/^{4}He ratios. However, for tritium to significantly affect the ^{3}He/^{4}He ratios, the fluids would have to contain a
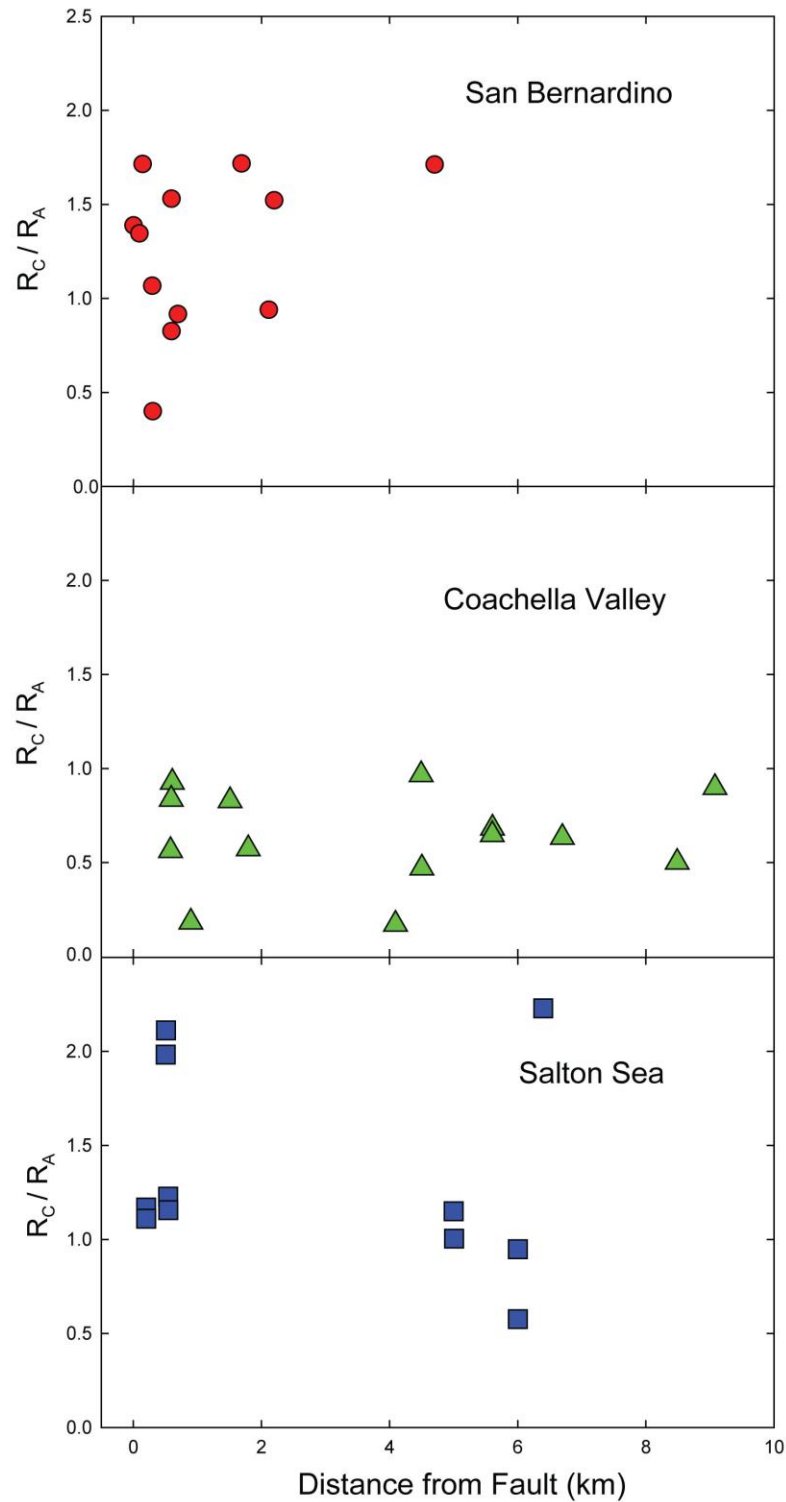
Figure 5.2.1: Plot of helium isotope ratios corrected for air-bubble entrainment and air saturated water (R_C) normalized to ^{3}He/^{4}He ratio of air (R_A) versus distance from any fault.

substantial fraction of 1963 precipitation (from nuclear bomb testing in the

atmosphere) and the aquifer system would have had to remain a closed system since

that time (Hilton et al., 2000). San Bernardino's aquifer system is predominantly old

water (~1,000 - 40,000 years; Woolfenden and Kadhim, 1997), so it likely has only a

very small portion of 1963 precipitation, if any. Conversely, Salton Trough (consisting

of the Salton Sea and Coachella Valley) groundwater is predominantly ~10-40 years

old (Kelliher, 2006; Goldrath, 2007), which is too young to contain a significant

portion of 1963 precipitation.

Second, the ^{6}Li (n,α) ^{3}H $\rightarrow$ ^{3}He reaction in the aquifer matrix can also affect the

^{3}He/^{4}He ratio; however, the concentrations of Li would need to be unrealistically large

within the aquifer rock to contribute to the higher ^{3}He/^{4}He values (Kulongoski et al.,

2005). Assuming a Li concentration of 50 ppm, an upper limit for sedimentary rocks

(Andrews, 1985), the calculated ^{3}He/^{4}He ratio would be 2.58 x 10^{-8} or 0.02 R$_A$

(Kulongoski et al. 2003), much lower than any of the observed ^{3}He/^{4}He ratios in this

study.

Third, another potential significant contributor to the observed variability in

^{3}He/^{4}He ratios is dilution with older waters characterized by high ^{4}He concentrations.

The U/Th decay within the aquifer matrix contributes more ^{4}He to the system as time

progresses, so the mantle helium ratio signal is diluted. San Bernardino Basin contains

relatively old water which varies in age from ~1,000 to 40,000 years (Woolfenden and

Kadhim, 1997) and the range of measured ^{4}He concentrations is 0.320 – 478 (x 10^{-7}

cm^3 STP/g) (Table 1). Using a ^{4}He production value of 5.01 x 10^{-13} cm^3 STP/g/yr

(calculated from U = 2.3 ppm; Th = 7.9 ppm; at an assumed porosity of 20%;

Kulongoski et al., 2005), the range of ^{4}He concentrations from U/Th decay in San

Bernardino groundwaters from U/Th decay is ~0.005 – 0.2 (x 10^{-7} cm^3 STP/gH$_2$O)

(1,000 to 40,000 years). So, ^{4}He produced from U/Th decay does not provide an

explanation for the variability seen within the San Bernardino Basin. The age of

groundwater in the Salton Trough is on the order of tens of years (Kelliher, 2006;

Goldrath, 2007), so there only a small amount of radiogenic helium present in the

groundwaters to affect ^{3}He/^{4}He ratios.

Fourth, helium-rich water from sub-regional flow cells (depths of ~500-1000

m) has been suggested to affect the helium isotope ratios (Bethke el al., 2000;

Kulongoski et al. 2013). Indeed, both the Salton Trough and San Bernardino Basin

contain deep basins, with the basement/sediment interfaces at 5-6 km (Fuis et al.,

1982) and >1200 km (Danskin, 2005), respectively. It is likely that any flow-cells are

restricted in size due to the numerous fault traces found within each sedimentary basin

so that any helium-rich water circulation within the aquifer would be severely

restricted (Wallace, 1990; Danskin, 2005). Due to the numerous fault traces found in

the area, basal flow of helium-rich fluids is obstructed because the flow is restricted.

Other possibilities to explain variations in ^{3}He/^{4}He ratios in the San Bernardino

Basin and Salton Trough include helium-rich fluid transport via smaller fractures and

faults within the sediment of the basin (Torgerson and O'Donnell, 1991) or re-

distribution of mantle-helium upward flow by sediment overlying the fractured

basement rock. Fluid transport via smaller fractures and faults is a very likely cause of

the observed spatial variations of $^3He/^4He$ ratios, especially in the San Bernardino Basin, as there are many smaller faults and fractures to direct flow to some areas in the basin and not to others. Within the Salton Trough, however, the more dominant feature is most likely re-distribution of helium via overlying sediment, because there are not as many smaller faults and fractures within the Salton Trough compared to the San Bernardino Basin. The distribution of the helium could be greatly affected by 5-6 km of overlying sediment that fills the trough. As the mantle-helium traverses the sediment basin, it could preferentially choose certain porous pathways to travel to the groundwater. Combined with the possibility of small fractures directing flow, this could lead to the observed large spatial variability of the $^3He/^4He$ ratios observed in both the Salton Trough and San Bernardino Basin.

In summary, the most probable causes of the $^3He/^4He$ ratio variability observed over short distances are (1) restriction of flow by fault traces, (2) helium-rich fluid transport via fractures and faults, and (3) re-distribution of mantle-helium by overlying sediment.

5.3. CO_2 provenance along SAFS

In this section, the origin of CO_2 within groundwaters of the three sampling regions is considered. The total dissolved inorganic carbon (TDIC or DIC) is comprised of two components: carbon associated dissolution of carbonates within the aquifer system (C_{carb}) and CO_2 from other (external) sources (C_{ext}). The external CO_2 can be further resolved into organic carbon (C_{org}) and deep-seated or endogenic carbon

(C_{endo}) (Figure 5.3.1). The methodology of resolving CO_2 into these various components is described in *Appendix 7.2* and is adopted from Chiodini et al. (2000; 2004), and Crossey et al. (2009).
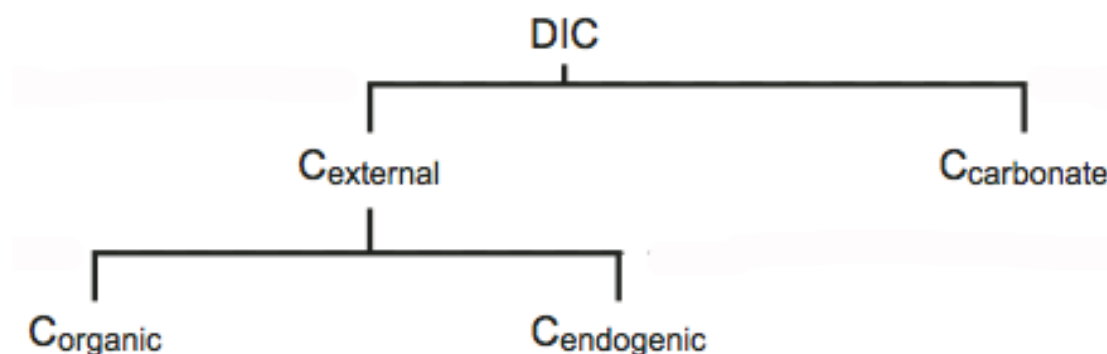
Figure 5.3.1: Constituents of TDIC. Image adopted and modified from Chiodini et al. 2000, Chiodini et al. 2004, and Crossey et al. 2009

Table 3 shows the calculated percentages of carbon provenance using equations described in *Appendix 7.2*. The San Bernardino groundwater contains C_{carb} contributions ranging from 14.7 – 49.4%. The median carbonate contribution to San Bernardino groundwaters is 40.3% (n =12). As described by Dutcher and Garrett (1963), the basin and surrounding mountains are rich with recrystallized limestone. The large contribution of C_{carb} in the groundwaters is consistent with this observation.

Dissolved inorganic carbon within the Salton Sea groundwaters contains a much less significant carbonate contribution. The C_{carb} contribution ranges from 0.0 – 39.1% (median = 18.5%; n = 11). The basin is filled with Quaternary wash and fill from the surrounding igneous and metamorphic mountains, which do not contain a significant amount of carbonate-rich rocks (Wallace, 1990). Hence, a lower carbonate contribution is expected.

Lastly, Coachella Valley groundwaters have the lowest carbonate contribution (median = 0%; n = 14). However, there are only six of the 14 samples that have the major ion chemistry data necessary to calculate C_{carb}. Although, C_{carb} in four out the six analyzed samples is 0%, so an assumed 0% value for the remaining eight unanalyzed samples within Coachella Valley was used for the calculations. The geology in Coachella Valley is very similar to Salton Sea, so, again, the low carbonate contribution is expected (Wallace, 1990).

The C_{ext} values of San Bernardino groundwaters are the lowest in this study, which are due to the high carbonate contribution. Meanwhile, the carbon within Salton Trough groundwater samples contains high proportions of C_{ext}. To further determine the source of carbon, C_{ext} is resolved into C_{org} and C_{endo} components (Chiodini et al. 2000; Figure 5.3.1). To determine the respective contributions of organic and endogenic (deep) sources, Figure 7.2.2 is described in *Appendix 7.2*, following the approach of Chiodini et al. (2000; 2004), and Crossey et al. (2009). Figure 5.3.2 is used to determine the carbon provenance of the CO_2 by plotting C_{ext} vs $\delta^{13}C_{ext}$. Reference lines are placed upon the figure at 10% and 50% endogenic contributions for comparison. The methodology is described in *Appendix 7.2*. As observed in the plot, San Bernardino groundwaters have the lowest endogenic contribution (median = 32.8%); in fact, all samples except one fall below the 50% endogenic contribution line. Organic sources dominate the contribution in the San Bernardino Basin groundwaters. The low $\delta^{13}C_{ext}$ values of San Bernardino groundwaters is probably due to vegetative soil CO_2 contributions which would first

dissolve during infiltration in the recharge areas (Chiodini et al. 2004). As described in *section 2.2*, the recharge of San Bernardino Basin is mostly from seepage and runoff from the surrounding San Gabriel and San Bernardino mountains, which, indeed, are highly vegetated (Woolfenden and Kadhim, 1997). Additionally, organic shales have been observed at ~3500 m below the surface in the San Andreas Fault Observatory at Depth (SAFOD) in central California. These same organic shales are argued as a source of carbon contribution along the SAFS along the Big Bend section also (Kulongoski et al., 2013). The low $\delta^{13}C_{ext}$ values could be, in part, attributed to these organic shales.

The endogenic contribution of the Coachella Valley groundwaters is relatively high (median = 78.8%). The deep sourcing could be attributed to the pull-apart basin found south of the Salton Sea. However, there are three groundwater samples that fall above the mixing curves, showing that there is some other factor which is not represented by the binary mixing curve. A three-endmember mixing diagram adopted from Sano and Marty (1995) is discussed later in *section 5.5* and outlined in *Appendix 7.3*, which could explain this phenomenon.

Finally, Salton Sea groundwaters have the highest endogenic contribution (median = 81.2%). This is to be expected, as there is the pull-apart basin at the south end of the Salton Sea, which contributes magmatic gases and fluids to the system (Fuis et al., 1982; Wallace, 1990).

Table 3: Carbon provenance calculations.

Location	DIC mol/L	δ¹³C (DIC)[b] vs PDB	C_{carb}[c] mol/L	C_{carb}[d] %	C_{ext} mol/L	C_{ext}[d] %	δ¹³C_{ext} vs PDB	Endogenic[e] %	CO$_2$/³He x 10¹⁰	CO$_{2\,endo}$/³He x 10¹⁰
Salton Sea										
Pacific Aquafarms	0.0121	-8.67	0.0022	18.5	0.0098	81.5	-11.10	79.67	24.8	19.8
Pacific Aquafarms - 2	0.0095	-7.84	0.0027	28.5	0.0068	71.5	-11.76	77.47	39.9	30.9
Bashford's Spa	0.0089	-8.23	0.0022	25.2	0.0066	74.8	-11.67	77.77	19.0	14.8
Bashford's Spa - 2	0.0071	-7.96	0.0028	39.1	0.0043	60.9	-14.35	68.84	20.4	14.0
Fountain of Youth Campground	0.0171	-8.22	0.0034	19.9	0.0137	80.1	-10.77	80.77	13.3	10.7
Fountain of Youth Campground - 2	0.0163	-7.67	0.0037	22.6	0.0126	77.4	-10.50	81.66	14.4	11.8
Well T7A	0.0031	-6.36	0	0.0	0.0031	100	-6.36	95.48	64.6	61.7
Well T7A- 2	0.0042	-7.97	0	0.0	0.0042	100	-7.97	90.11	3.06	2.76
Well T5	0.0076	-10.04	0	0.0	0.0076	100	-10.04	83.19	153	127
Cox Oasis	0.003	-10.65	0	0.0	0.0030	100	-10.65	81.18	24.9	20.2
Cox Oasis - 2	0.0032	-8.11	0	0.0	0.0032	100	-8.11	89.63	28.8	25.8
Coachella Valley[a]										
Eisenhower MC1	0.0028	-11.50	0.0012	45.1	0.0015	54.9	-22.58	41.39	18.6	7.70
WCAS Dillon #1	0.0014	-9.20	0	0.0	0.0014	100	-9.20	86.00	2.88	2.48
Grant St Farm	0.0024	-4.60	0	0.0	0.0024	100	-4.60	--[f]	19.0	19.0
Grant St. Farm-R	0.0023	-4.70	n.a.	0.0	0.0023	100	-4.70	--[f]	17.4	17.4
MSWD27	0.0026	-12.10	0.0005	18.1	0.0021	81.9	-15.22	65.92	21.9	14.4
MSWD 27-R	0.0024	-12.80	n.a.	0.0	0.0024	100	-12.80	74.00	22.4	16.6
MSWD 29	0.0028	3.45	0	0.0	0.0028	100	3.45	--[f]	20.4	20.4
MSWD 31	0.0019	-13.83	n.a.	0.0	0.0019	100	-13.83	70.57	6.70	4.73
MSWD 24	0.0035	-10.50	n.a.	0.0	0.0035	100	-10.50	81.67	43.8	35.8
CVWD 6807-1	0.0012	-11.35	n.a.	0.0	0.0012	100	-11.35	78.83	10.7	8.44
CVWD 6805	0.0013	-12.44	n.a.	0.0	0.0013	100	-12.44	75.20	10.0	7.52
CVWD 4722	0.0015	-11.03	n.a.	0.0	0.0015	100	-11.03	79.90	30.8	24.6
CVWD 4563	0.0008	-11.00	n.a.	0.0	0.0008	100	-11.00	80.00	10.8	8.64
WCAS Airport Well	0.001	-10.24	0	0.0	0.0010	100	-10.24	82.53	7.60	6.27
San Bernardino										
Olive and Garner Street Well	0.0036	-11.78	0.0015	41.4	0.0021	58.6	-21.52	44.94	124	55.7
Lytle Creek 02	0.0023	-16.81	0.0008	36.7	0.0014	63.3	-27.71	24.29	52.9	12.9
Newmark #1	0.0033	-13.98	0.0013	39.5	0.0020	60.5	-24.43	35.24	84.3	29.7
Devil's Canyon 06	0.0042	-12.57	0.0015	35.7	0.0027	64.3	-20.64	47.87	200	95.7
Kenwood #2	0.0048	-16.34	0.0017	34.3	0.0032	65.7	-25.89	30.37	78.1	23.7
40th and Valencia	0.0033	-13.33	0.0005	14.7	0.0028	85.3	-15.97	63.43	182	115
Waterman Well	0.0041	-13.01	0.0017	41.0	0.0024	59.0	-23.43	38.56	50.7	19.5
Rialto No. 24	0.0026	-15.21	0.0013	48.6	0.0013	51.4	-31.49	11.70	37.3	4.36
Rialto No. 54	0.0026	-16.31	0.0013	49.4	0.0013	50.6	-34.22	2.61	3.10	0.08
Rialto No. 2	0.0022	-15.78	0.0010	47.7	0.0011	52.3	-32.00	10.00	25.4	2.54
Rialto No. 7	0.0029	-13.92	0.0010	36.0	0.0018	64.0	-22.87	40.43	31.1	12.6
Rialto No. 42	0.0031	-14.64	0.0014	43.7	0.0017	56.3	-27.57	24.76	67.7	16.8

[a]Calculated using data from USGS (pers. comm. J. Kulongoski, USGS)

[b]Error = ± 0.5‰

[c]Calculated using methodology from Chiodini et al. (2004) and Crossey et al. (2009). See Appendix

[d]Percentage of total DIC.

[e]Percentage of calculated DIC

[e]Calculated using plot adapted from Chiodini et al. (2004) and Crossey et al. (2009)(Figure 4). See Appendix

[f]Falls above binary mixing lines (>100% endogenic contribution)
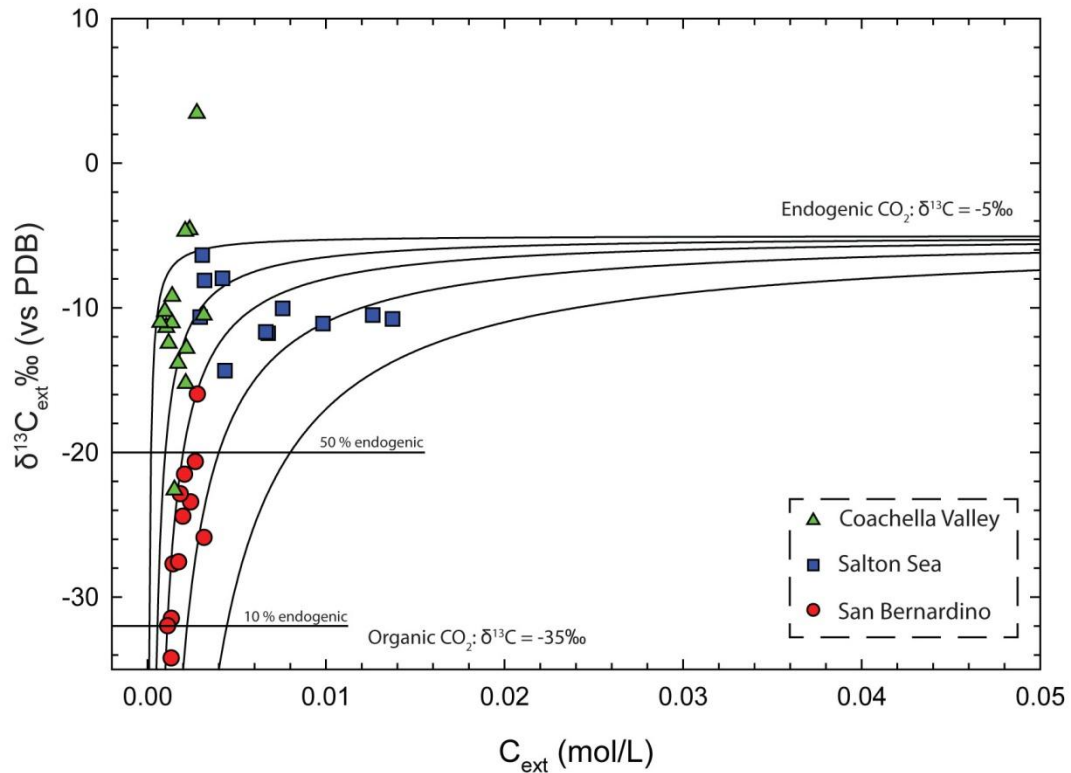
Figure 5.3.2: Plot of C_{ext} vs $\delta^{13}C_{ext}$ ‰ (vs PDB) in groundwaters in the San Bernardino Basin and the Salton Trough. C_{ext} is the dissolved carbon from endogenic and organic sources. Mixing curves connect two endmembers $\delta^{13}C_{endo}$ = -5‰ and $\delta^{13}C_{org}$ = -35‰. Horizontal lines show 10% and 50% endogenic CO_2. Adopted from Chiodini et al. (2000; 2004), and Crossey et al. (2009).

5.4. $CO_2/^3He$ ratios and endogenic contribution

Fluids rich in CO_2 have been suggested as a carrier for volatiles, like helium, from the mantle (Dunai and Porcelli, 2002). CO_2 is more abundant in the mantle than helium by a factor of 10^4 (O'Nions and Oxburgh, 1988). However, both helium and CO_2 are released in similar scenarios, but are not necessarily coupled during every stage of transport (Dunai and Porcelli, 2002). Because a portion of the helium is expected to be of mantle origin, some of the CO_2 can also be assumed to have deep, or endogenic, sourcing. Therefore, $CO_{2\ endogenic}/^3He$ values have been calculated using the

approach illustrated in Figure 5.3.2 in order to better constrain the contribution of the

deep CO_2 component.

By subtracting C_{carb} and C_{org} from DIC, the $CO_{2\,endogenic}/{}^3He$ ratio can be

determined assuming all the ${}^3He$ is endogenic (Table 3). The $CO_{2\,endogenic}/{}^3He$ values in

Coachella Valley groundwaters are the lowest (median $= 1.15\,\text{x}10^{11}$), Salton Sea

groundwaters have the highest (median $= 1.98\,\text{x}\,10^{11}$), and San Bernardino

groundwaters are intermediate (median $= 1.82\,\text{x}\,10^{11}$). However, despite the large

variations in C_{org} between the different study areas, all regions have relatively similar

median $CO_{2\,endogenic}/{}^3He$ values, between 1- 2 ($\text{x}\,10^{11}$) and they all fall on the lower

end of continental values ($10^{11} - 10^{14}$). A typical endogenic (deep) $CO_2/{}^3He$ value is

$\sim 2\text{x}10^9$, assuming that the lithospheric mantle resembles the upper mantle in regards to

carbon and helium (Marty and Jambon, 1987). So, as these gases have travelled to the

surface, there has clearly been crustal contamination, increasing the $CO_2/{}^3He$ ratio

(O'Nions and Oxburgh, 1988).

5.5. Ternary mixture to determine carbon provenance.

An alternate approach to determine carbon provenance is described in

Appendix 7.3. In this scenario, the C_{carb} portion is first subtracted from DIC to

determine C_{ext}, similar to the above binary mixing plot. Then the remaining CO_2 (C_{ext})

is assumed to comprise a ternary mixture of organic sediment- (S), limestone- (L), and

mantle-derived (M) CO_2. The proportions of CO_2 derived from each of these three end

members (M, L, and S) can be calculated using the $\delta^{13}C_{ext}$ and $CO_2/{}^3He$ following the

approach of Sano and Marty (1995) (Figure 5.5.1). These calculations are shown in

Table 4.

In the Salton Trough (Coachella Valley and Salton Sea) groundwater samples,

the CO_2 provenance is dominated by marine carbonate (L) inputs (median = 68.4%).

This disagrees with findings from other studies along the SAFS (Wiersberg and

Erzinger, 2011; Kulongoski et al., 2013) that attribute the source of SAFS fluids to

metamorphism of organic-rich shale as a major source of CO_2. The organic-rich shale

unit, however, is not found as far south as the Salton Trough, so this is to be expected

(Wallace, 1990).
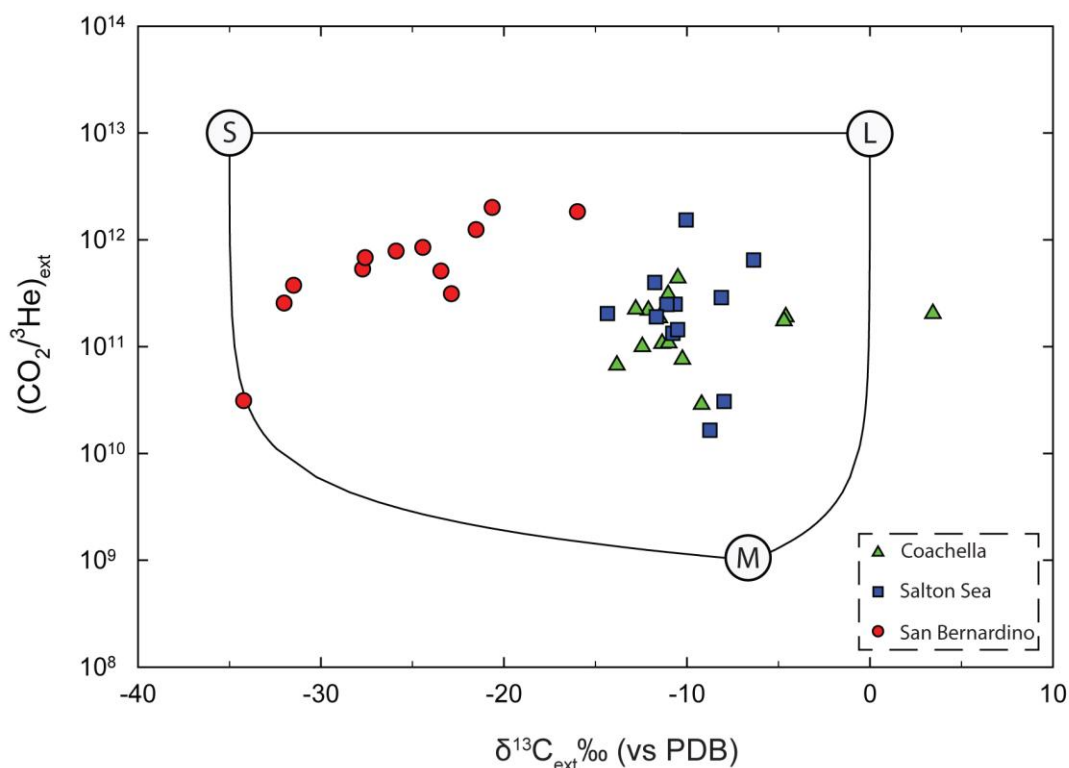
Figure 5.5.1: Plot of $CO_2/^3He$ vs $\delta^{13}C_{ext}$ ‰ (vs PDB) for sampled groundwaters in the San Bernardino Basin and the Salton Trough. Mantle "M" values: $\delta^{13}C_{ext}$ = -6.5‰; $CO_2/^3He$ = 2x10^9. Marine carbonate "L" values: $\delta^{13}C_{ext}$ = 0‰; $CO_2/^3He$ = 1x10^13. Organic sediment "S" values: $\delta^{13}C_{ext}$ = -35‰; $CO_2/^3He$ = 1x10^13. Adopted from Sano and Marty (1995) and Kulongoski et al. (2013).

San Bernardino samples display a much larger organic sediment (S) carbon input (median = 71.9%), similar to the aforementioned previous studies (Wiersberg and Erzinger, 2011; Kulongoski et al., 2013). The large organic inputs could also be attributed to the increased vegetation seen throughout the recharge areas of the San Bernardino Basin (Dutcher and Garrett, 1963). Also, San Bernardino groundwaters have low relative mantle CO_2 input (median = 0.24%), again, probably because the CO_2 provenance is dominated by the vegetation in the recharge areas.

Furthermore, Salton Sea and Coachella Valley samples have higher median mantle CO_2 contributions (0.50% and 0.74%, respectively), compared to San Bernardino (0.24%). This is likely due to the pull-apart basin found in the southern portion of the Salton Trough contributing mantle gases to the system (Fuis et al., 1984; Wallace, 1990).

5.6. Mixing model comparison.

The two mixing models described in *sections 5.3* and *5.5* produce very different mantle contribution percentages. For groundwaters from Pacific Aquafarms in the Salton Sea, for example, the binary mixing (Chiodini et al., 2000; 2004; Crossey et al., 2009) model predicts that there is 79.7% endogenic (deep) contribution ($\delta^{13}C$ = -5‰). However, the ternary mixing model (Sano and Marty, 1995) predicts that there is only 0.49% mantle contribution ($\delta^{13}C$ = -6.5‰).

The approach described by Chiodini et al. (2000; 2004) and used by Crossey et al. (2009) proclaims that all of the carbonate (limestone) addition to the carbon is

Table 4: Carbon provenance calculations using ternary mixture from Sano and Marty (1995).

Location	DIC (mol/L)	$\delta\,^{13}C$ (DIC)[b]	C_{carb} (mol/L)[c]	C_{carb}[d] %	C_{ext} (mol/L)	C_{ext}[d] %	$\delta\,^{13}C_{ext}$	$CO_2/^3He$ x 10^{10}	L_{ext}[e] %	S_{ext}[f] %	M_{ext}[g] %
Salton Sea											
Pacific Aquafarms	0.0121	-8.67	0.0022	18.5	0.0098	81.5	-11.10	24.8	67.9	31.6	0.49
Pacific Aquafarms - 2	0.0095	-7.84	0.0027	28.5	0.0068	71.5	-11.76	39.9	66.1	33.5	0.34
Bashford's Spa	0.0089	-8.23	0.0022	25.2	0.0066	74.8	-11.67	19.0	66.1	33.2	0.69
Bashford's Spa - 2	0.0071	-7.96	0.0028	39.1	0.0043	60.9	-14.35	20.4	58.4	40.8	0.79
Fountain of Youth Campground	0.0171	-8.22	0.0034	19.9	0.0137	80.1	-10.77	13.3	68.5	30.6	0.93
Fountain of Youth Campground	0.0163	-7.67	0.0037	22.6	0.0126	77.4	-10.50	14.4	69.3	29.8	0.89
Well T7A	0.0031	-6.36	0.0000	0.00	0.0031	100	-6.36	64.6	81.7	18.1	0.14
Well T7A- 2	0.0042	-7.97	0.0000	0.00	0.0042	100	-7.97	3.06	74.6	22.2	3.26
Well T5	0.0076	-10.04	0.0000	0.00	0.0076	100	-10.04	153.0	71.3	28.7	0.06
Cox Oasis	0.0030	-10.65	0.0000	0.00	0.0030	100	-10.65	24.9	69.3	30.3	0.39
Cox Oasis - 2	0.0032	-8.11	0.0000	0.00	0.0032	100	-8.11	28.8	76.6	23.1	0.34
Coachella Valley[a]											
Eisenhower MC1	0.0028	-11.50	0.0012	45.1	0.0015	54.9	-22.58	18.6	34.7	64.3	0.97
WCAS Dillon #1	0.0014	-9.20	0.0000	0.00	0.0014	100	-9.20	2.88	70.9	25.6	3.46
Grant St Farm	0.0024	-4.60	0.0000	0.00	0.0024	100	-4.60	19.0	86.4	13.0	0.52
Grant St. Farm-R	0.0023	-4.70	n.a.	0.00	0.0023	100	-4.70	17.4	86.1	13.3	0.56
MSWD27	0.0026	-12.10	0.0005	18.1	0.0021	81.9	-15.22	21.9	56.1	43.4	0.55
MSWD 27-R	0.0024	-12.80	n.a.	0.00	0.0024	100	-12.80	22.4	63.1	36.5	0.44
MSWD 29	0.0028	3.45	0.0000	0.00	0.0028	100	3.45	20.4	99.5	--[h]	0.48
MSWD 31	0.0019	-13.83	n.a.	0.00	0.0019	100	-13.83	6.70	59.3	39.2	1.48
MSWD 24	0.0035	-10.50	n.a.	0.00	0.0035	100	-10.50	43.8	69.8	30.0	0.22
CVWD 6807-1	0.0012	-11.35	n.a.	0.00	0.0012	100	-11.35	10.7	66.8	32.3	0.92
CVWD 6805	0.0013	-12.44	n.a.	0.00	0.0013	100	-12.44	10.0	63.7	35.4	0.99
CVWD 4722	0.0015	-11.03	n.a.	0.00	0.0015	100	-11.03	30.8	68.2	31.5	0.31
CVWD 4563	0.0008	-11.00	n.a.	0.00	0.0008	100	-11.00	10.8	67.8	31.3	0.92
WCAS Airport Well	0.0010	-10.24	0.0000	0.00	0.0010	100	-10.24	7.60	69.7	29.0	1.31
San Bernardino											
Olive and Garner Street Well	0.0036	-11.78	0.0015	41.4	0.0021	58.6	-21.52	124	38.4	61.5	0.13
Lytle Creek 02	0.0023	-16.81	0.0008	36.7	0.0014	63.3	-27.71	52.9	20.6	79.1	0.29
Newmark #1	0.0033	-13.98	0.0013	39.5	0.0020	60.5	-24.43	84.3	30.1	69.8	0.19
Devil's Canyon 06	0.0042	-12.57	0.0015	35.7	0.0027	64.3	-20.64	200	20.6	79.1	0.29
Kenwood #2	0.0048	-16.34	0.0017	34.3	0.0032	65.7	-25.89	78.1	30.1	69.8	0.19
40th and Valencia	0.0033	-13.33	0.0005	14.7	0.0028	85.3	-15.97	182	41.0	59.0	0.07
Waterman Well	0.0041	-13.01	0.0017	41.0	0.0024	59.0	-23.43	50.7	25.9	73.9	0.18
Rialto No. 24	0.0026	-15.21	0.0013	48.6	0.0013	51.4	-31.49	37.3	54.3	45.6	0.05
Rialto No. 54	0.0026	-16.31	0.0013	49.4	0.0013	50.6	-34.22	3.10	32.8	66.9	0.32
Rialto No. 2	0.0022	-15.78	0.0010	47.7	0.0011	52.3	-32.00	25.4	9.6	89.9	0.51
Rialto No. 7	0.0029	-13.92	0.0010	36.0	0.0018	64.0	-22.87	31.1	--[i]	93.6	6.37
Rialto No. 42	0.0031	-14.64	0.0014	43.7	0.0017	56.3	-27.57	67.7	8.0	91.3	0.74

[a] Calculated using data from USGS (pers. comm. J. Kulongoski, USGS)

[b] Error = ± 0.5‰

[c] Calculated using methodology from Chiodini et al. (2004) and Crossey et al. (2009). See Appendix

[d] Percentage of total DIC.

[e,f,g] Calculated using ternary mixing plot (Figure 5)

[e] Assumed $\delta\,^{13}C = 0$‰ ; $CO_2/^3He = 1 \times 10^{13}$

[f] Assumed $\delta\,^{13}C = -35$‰ ; $CO_2/^3He = 1 \times 10^{13}$

[g] Assumed $\delta\,^{13}C = -6.5$‰ ; $CO_2/^3He = 1 \times 10^{9}$

[h] Falls on binary mixing line between M and L, so S is at 0%

[i] Falls on binary mixing line between M and S, so L is at 0%

subtracted from the DIC using the Ca, Mg, and SO_4 concentrations within the aquifer. However, upon comparison with the ternary mixture model described by Sano and Marty (1995), it is evident that there is indeed an addition of carbon with a limestone isotopic signature that occurs much deeper than in the aquifer itself, one that is not affected by the water chemistry subtractions.

Operating within the ternary mixing model, groundwaters from Pacific Aquafarms, for instance, have a CO_2 mantle contribution of 0.49% and a marine carbonate contribution of 67.9% (Table 4). Compared with the binary mixing model prediction of endogenic contribution, 79.7% (Table 3), it seems that the endogenic portion from the binary mixing model almost completely encompasses both mantle (M) and marine carbonate (L) contributions predicted by the ternary mixing model. So, if the binary mixing model would have been used alone, the conclusion would be that a large portion of the carbon is mantle derived when, in fact, that large percentage captures the deep marine carbonate contribution in addition to the mantle contribution.

These two methods of determining carbon provenance are not equal or interchangeable, as evidenced above. The binary mixing model underestimates the contribution of the marine carbonates (limestone) inputs while overestimating the endogenic, or mantle inputs. This is because this model operates under the assumption that by using the water chemistry calculations, all of the carbonate (C_{carb}) contribution has been subtracted. This assumption is misguided because it is not able to accurately calculate the proper contribution percentages. The ternary model also makes a few assumptions. This model assumes $CO_2/{}^3He$ and $\delta^{13}C$ values for the marine carbonate

(L) and sedimentary (S) and mantle (M) endmembers. The sedimentary endmember

has a very large range of $\delta^{13}C$ values, which can drastically change the calculated

carbon provenance percentages. Also, the mantle endmember value of $CO_2/^3He$ (2 x

10^9) is calculated from direct sampling at MOR, however to assume this value for

lithospheric degassing might not be the most appropriate.

5.7. Calculating volatile fluxes

Kennedy et al. (1997) calculated an upward fluid flow rate through the SAFS,

using the aforementioned 1-dimensional model (*section 5.1*) where crustal ^4He dilutes

mantle $^3He/^4He$ ratios. Based on a 30 km crustal thickness (H_C), a composition of a

well in central California with $[He]_{F,m}$ = 426.0 x 10^{-7} cm^3 STP/g fluid (air corrected

mantle He concentration), and $^3He/^4He$ = 2 R_A, they estimated a flow rate (q) of ~3

mm/year (upper and lower limits of 10.5 and 1 mm/yr) using the following equation:

$$q = \frac{H_C \, P(He)\rho_s}{\rho_f[He]_{F,m}} \times \left[\frac{R_s - R_c}{R_m - R_s}\right]$$

where ρ_s and ρ_f are the densities of solid and fluid phases, P(He) is the present-day ^4He

production rate from U/Th, and R is the $^3He/^4He$ ratio of the sample (*s*), crust (*c*), and

mantle (*m*). In contrast, Kulongoski et al. (2013) calculated fluid flow rates of ~147

mm/year for the Big Bend section of the SAFS based on 30 km crustal thickness,

P(He) = 5.01 x 10^{-13} cm^3 STP/g/a, ρ_s = 2.8 g/cm^3, $He_{F,m}$ = 2.25 x 10^{-7} cm^3 STP/g fluid

and sample R_s = $^3He/^4He$ = 3.52 R_A. The flow rate of Kulongoski et al. (2013) for the

Big Bend section of the SAFS is much higher as the measured $^3He/^4He$ ratio was much

higher in this section

The highest ^{3}He/^{3}He ratio in this study is found at Well T5 in the Salton Sea at 2.23 R$_A$, with a [^{4}He]$_{F,m}$ = 0.135 (x 10^{-7} cm^3 STP/g H$_2$O). Using an assumed 30 km crustal thickness, P(He) = 5.01 x 10^{-13} cm^3 STP/g/a, and ρ_s = 2.8 g/cm^3, the calculated upward fluid flow rate in the Salton Sea is ~1190 mm/year. In the Coachella Valley, the upward fluid flow rate is ~395 mm/year, using CVWD 4563 with a [^{4}He]$_{F,m}$ = 0.144 (x 10^{-7} cm^3 STP/g H$_2$O) and 0.97 R$_A$. Finally, the upward fluid flow rate in San Bernardino is ~622 mm/year, using Rialto No. 24 with a [^{4}He]$_{F,m}$ = 0.158 (x 10^{-7} cm^3 STP/g H$_2$O) and 1.53 R$_A$: other parameters are the same as in Kulongoski et al. (2013) and Kennedy et al. (1997).

The fluid flow rates of the three sampling areas in this study are all much higher than the previous studies by Kennedy et al. (1997) and Kulongoski et al. (2013). This is because along this stretch of the SAFS and SJFZ, the groundwaters have high ^{3}He/^{4}He ratios coupled with lower mantle helium concentrations. The elevated ^{3}He/^{4}He ratios and high fluid flow rates may characterize a permeable crust, most likely due to active fault behavior (Wallace, 1990), or, in the Salton Sea, the influence of pull-apart basin magma degassing (Fuis et al., 1982).

5.8. Flux estimates

To calculate the ^{3}He flux, the following equation from Kennedy et al. (1997) must be used:

$$\text{total } ^3\text{He flux} = q \times \rho_f \times [\text{He}_s] \times R_s$$

where q is upward fluid flux, ρ_f is the density of the fluid, $[He_s]$ is the helium-4

concentration of the sample, and R_s is the ^{3}He/^{4}He ratio of the sample. Kennedy et al.

(1997) assumed a flow rate of 4 mm/year for the SAFS and calculated a ^{3}He flux of

~4.05 (x 10^{-11} cm^3 STP/cm^2/year) (~2 x 10^{-15} mol/cm^2/year). Integrating this flux over

the entire SAFS (length = 1000 km; width = 350 km), Kennedy et al. (1997) estimated

a total ^{3}He flux of 1.42 x 10^5 cm^3 STP/year (~6 mol/year). Kulongoski et al. (2013)

used the calculated 147 mm/year for the SAFS and calculated a ^{3}He flux of 3.71 (x 10^{-11} cm^3 STP/cm^2/year), equivalent to 1.3 (x 10^5 cm^3 STP/year) over the entire SAFS.

However, as this study and the study by Kulongoski et al. (2013) suggest, the

mantle-helium signal is restricted to ~10 km of the main fault trace. So, instead of

assuming the SAFS width to be 350 km, Kulongoski et al. (2013) assumed it to be

only 20 km. With the dimension change and the higher upward fluid flux, Kulongoski

et al. (2013) calculated a total ^{3}He flux along the SAFS at 7.4 x 10^3 cm^3 STP/year

(0.33 mol ^{3}He/year). Using the highest fluid flow rate, 1190 mm/year found at Well

T5 the Salton Sea, and the same SAFS dimensions as Kulongoski et al. (2013), the

calculated total ^{3}He flux for the entire SAFS is 3.63 x 10^3 cm^3 STP/year (0.16 mol

^{3}He/year), or roughly half of the amount calculated by Kulongoski et al (2013). This

shows that the southern portion of the fault is much less active with respect to fault-

related degassing.

However, the three sampling areas along the SAFS in this study display

different flux estimates, so combining the flux estimates would be misleading.

Furthermore, instead of using the total SAFS dimensions (1000 km x 20 km), smaller,

segmented dimensions should be used to reflect the different sampling areas. The

Salton Sea area (80 km x 20 km) produces 291 cm^3 STP/year of ^{3}He (0.013 mol

^{3}He/year) using Well T5, Coachella Valley (100 km x 20 km) produces 130 cm^3

STP/year of ^{3}He (0.0058 mol ^{3}He/year) using CVWD 4563, and San Bernardino (50

km x 20 km) produces 111 cm^3 STP/year of ^{3}He (0.0050 mol ^{3}He/year) using Rialto

No. 24.

Additionally, the flux of both CO_2 and ^{3}He/km/year are calculated to better

understand the fluxes of volatiles through the SAFS (Figure 5.9.1). The ^{3}He flux

estimates are calculated first using the previously calculated mol ^{3}He/year and then

divided over the length of the segment. For instance, the Salton Sea segment of the

SAFS is 80 km and the calculated flux is 0.013 mol^{3}He/year. Then the flux is divided

by the length to get a flux per kilometer within that section (1.64 x 10^{-4} mol ^{3}He/

km/yr). The lengths of the Coachella Valley, San Bernardino, and Big Bend

(Kulongoski et al., 2013) were designated to be 100 km, 50 km, and 100 km,

respectively. A value of 527 mol ^{3}He/year (Bianchi et al., 2010) and a length of 65,000

km were used for the Mid Ocean Ridges.

To calculate the CO_2 fluxes, two methods were used. Method 1 multiplies the

^{3}He flux per kilometer by the mantle $CO_2/^3$He ratio of 2 x 10^9 (Marty and Jambon,

1987) to obtain the CO_2 flux per kilometer. For example, the ^{3}He flux of the Salton

Sea, 1.64 x 10^{-4} mol /km/yr, is multiplied by 2 x 10^9 to obtain a CO_2 flux of 324 x 10^3

mol/km/yr. Method 2, however, is more complex. The ^{3}He flux per kilometer is

multiplied by the measured $CO_2/^3$He ratio for that sample locality and then multiplied

by the percent contribution of mantle carbon to the DIC (see Table 4) to obtain the CO_2 flux per kilometer. For example, first the ^{3}He flux of the Salton Sea, 1.64×10^{-4} mol/km/yr, is multiplied by the measured $CO_2/^3$He ratio at Well T5 (1.53×10^{12}). Then, the resultant CO_2 flux per kilometer is multiplied by 0.055% to obtain a CO_2 flux of 148×10^3 mol CO_2/km/yr. A value of 2.2×10^{12} mol CO_2/year (Javoy et al., 1982) was used for the MOR.

The two methods of calculation depict similar trends and fluxes; however, each method makes its own assumptions. For method 1, a value of 2×10^9 is assumed to be the representative $CO_2/^3$He ratio for the mantle (Marty and Jambon, 1987). To use this number for lithospheric degassing might not be appropriate, as it is calculated for oceanic upper mantle. So method 2 is used, because a direct $CO_2/^3$He ratio was obtained at the sampling sites. However, to use this measured ratio, the percentage of mantle carbon within the DIC must also be determined (outlined in *section 5.5*). This assumes $CO_2/^3$He and δ^{13}C values for the marine carbonate (L) and sedimentary (S) and mantle (M) endmembers (Figure 5.5.1). So, both of these methods of carbon flux calculations rely on the assumption that homogeneity exists along the fault, and between lithospheric and MOR degassing. Method 1 flux estimates are roughly twice as large as method 2 flux estimates, and this is most likely because the $CO_2/^3$He ratio assumed for the mantle (2×10^9; Marty and Jambon, 1987) could be an overestimate for the lithospheric degassing $CO_2/^3$He ratio.
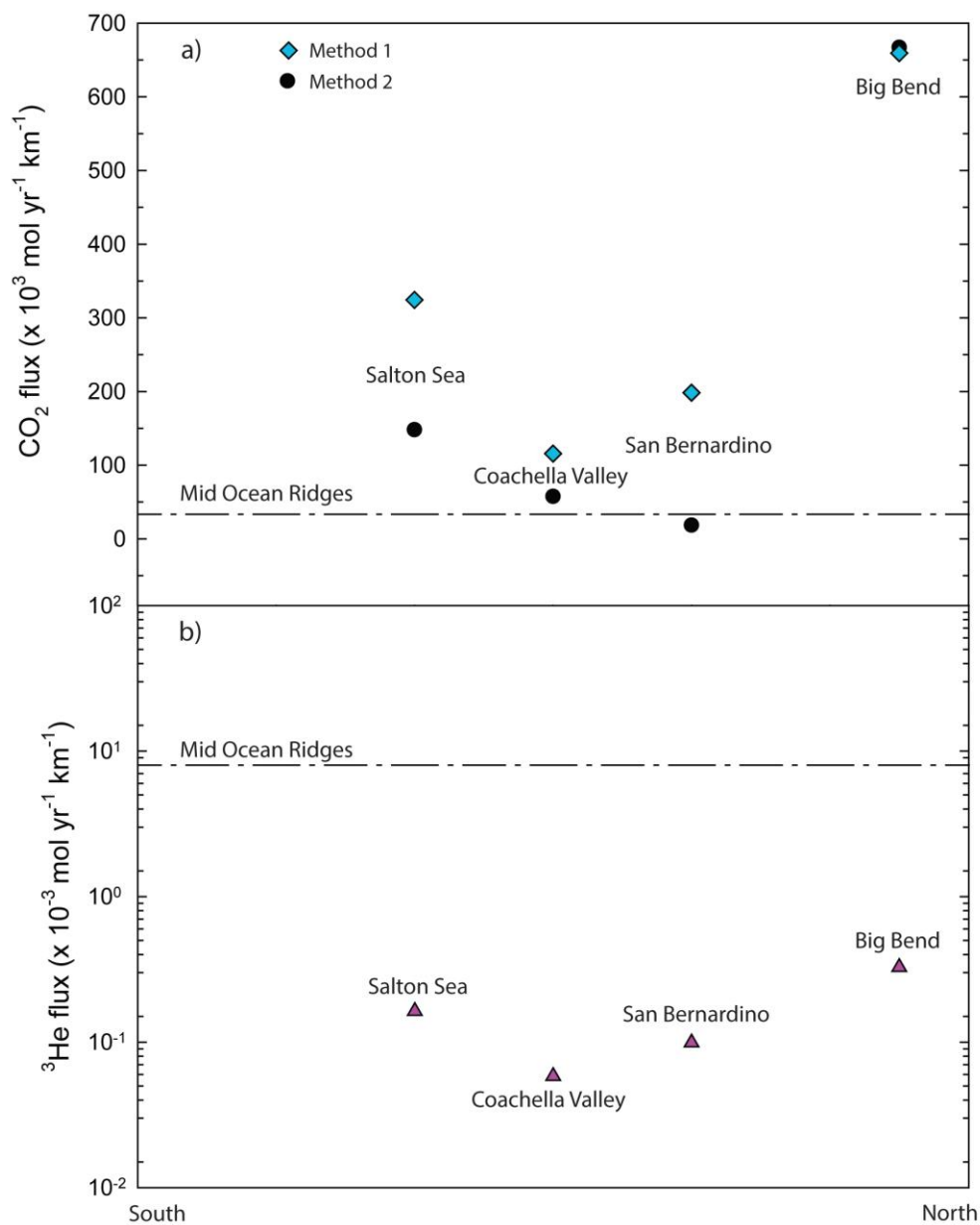
Figure 5.8.1: A plot of CO_2 and ^3He fluxes through various segments of the SAFS compared with a calculated flux through the worldwide system of Mid Ocean Ridges (MOR). A length of 65,000 km and values of 1000 mol ^3He/year (Craig et al., 1975) and 2.2 x 10^{12} mol CO_2/year (Javoy et al., 1982) were used for the MOR. A length of 100k m and values of 0.033 mol ^3He/year and 2.02 x 10^9 mol CO_2/year (Kulongoski et al., 2013) were used for the Big Bend section of the SAFS. The length of the Salton Sea segment is 80 km; Coachella Valley is 100 km; and San Bernardino is 50 km. On plot a), there were two separate methods used to calculate the CO_2 fluxes. Method 1 is shown with light blue diamonds. Method 2 is shown with black circles.

For reference, MOR CO_2 and [3]He fluxes have been included in Figure 5.8.1. The [3]He flux estimate of MOR is much higher than all of the segments of the southern SAFS. This is to be expected because MOR degassing has been proven to contribute large quantities of volatiles to the atmosphere through magmatic degassing (Craig and Clarke, 1970; Craig et al., 1975; Lupton et al., 1980; Marty and Tolsktikhin, 1998). However, the derived CO_2 fluxes of MOR (33.9 x 10^5 mol CO_2/year/km) are, in fact, less than or roughly equal to the flux estimates along the SAFS: Salton Sea = 324 x 10^5 mol CO_2/year/km or 148 x 10^5 mol CO_2/year/km, Coachella Valley = 115 x 10^5 mol CO_2/year/km or 57.5 x 10^5 mol CO_2/year/km, San Bernardino = 198 x 10^5 mol CO_2/year/km or 18.5 x 10^5 mol CO_2/year/km). So, the SAFS and other similar faults could be contributing significant CO_2 and should not be overlooked as a mantle volatile source in the atmosphere.

5.9. The transition from the EPR to the SAFS

Within this study, the Salton Sea has the highest CO_2 and He degassing fluxes, Coachella Valley has the lowest, and San Bernardino contains intermediate flux rates. The [3]He/[4]He ratio data also depict a similar trend. Figure 5.9.1 was constructed using [3]He/[4]He ratio data from this study and studies by Lupton et al. (1980), Mazzini et al. (2011), and Kulongoski et al. (2013). As the aforementioned degassing carbon fluxes suggest, there is little mantle contribution in the Coachella Valley, while the mantle involvement increases both to the north and to the south. Wallace (1990) describes a bend in the fault north of San Bernardino, which causes the thickening of the crust in
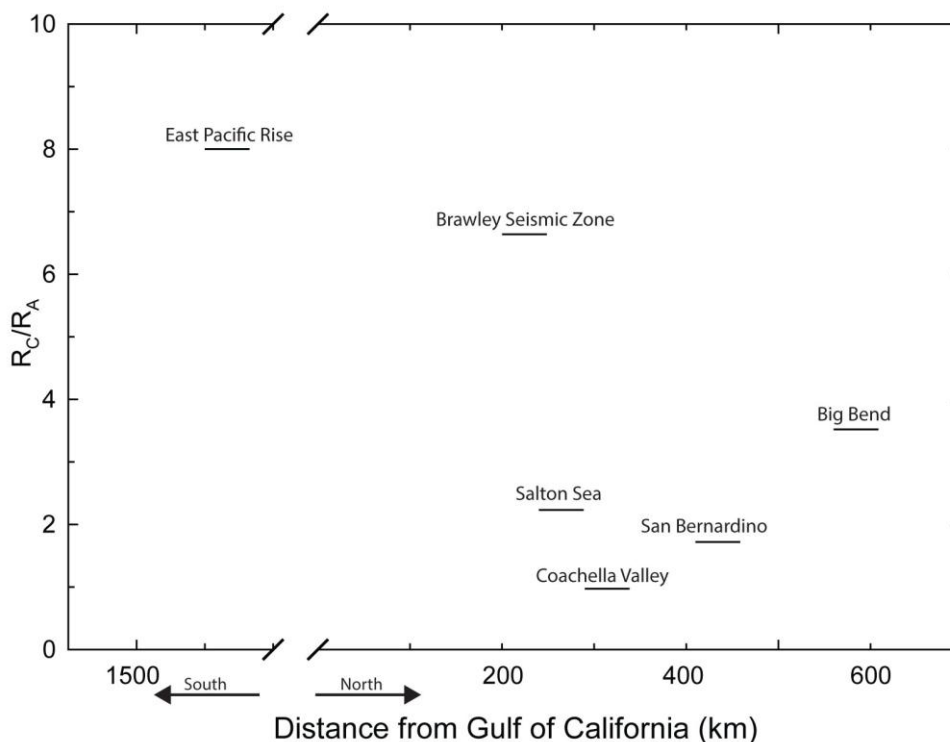
Figure 5.9.1: Plot of helium isotope ratios corrected for air saturated water and air-bubble entrainment (R_C) normalized to ^{3}He/^{4}He ratio of air (R_A) along the SAFS versus the distance along the fault from the northern most portion of the Gulf of California. East Pacific Rise ^{3}He/^{4}He ratio (Lupton et al., 1980). Brawley Seismic Zone ^{3}He/^{4}He ratio (Mazzini et al., 2011).

the Coachella Valley. This bend increases the distance that mantle gases have to travel, i.e. the crustal thickness is increased relative to adjacent segments, thus decreasing the amount of mantle involvement seen in groundwater near the surface. The Salton Sea would also have a lower flux if it were not for the rifting that occurs just to the south of the Salton Sea. This rifting thins the crust and contributes magma to relatively shallow parts of the crust, which also contributes to the elevated degassing fluxes and elevated ^{3}He/^{4}He ratios (Mazzini et al., 2011). So groundwaters from the Salton Sea, in fact, have higher degassing fluxes and ^{3}He/^{4}He ratios due to the rifting of the basin and not to enhanced leakage of mantle volatiles through the

SAFS. North of the Coachella Valley, in San Bernardino, the amount of mantle contribution is higher due to increased fault-related mantle degassing. Thus, the southernmost section of the SAFS (Coachella Valley and southward along the SAFS) represents a transition from fault-related degassing in the central and northern segments of the SAFS to rift-related degassing seen in the Salton Sea region.

*5.10. Earthquake activity relationships*

In Figure 5.10.1, recent (1900-present) earthquakes have been plotted on a map of southern California (US Geological Survey, 2013). The Coachella Valley segment (immediately north of the Salton Sea) contains no major earthquakes (M > 4), while both Salton Sea and San Bernardino sections have had numerous large earthquakes in recent history. Additionally, the Big Bend section and the Brawley Seismic Zone (BSZ) have experienced numerous earthquakes.
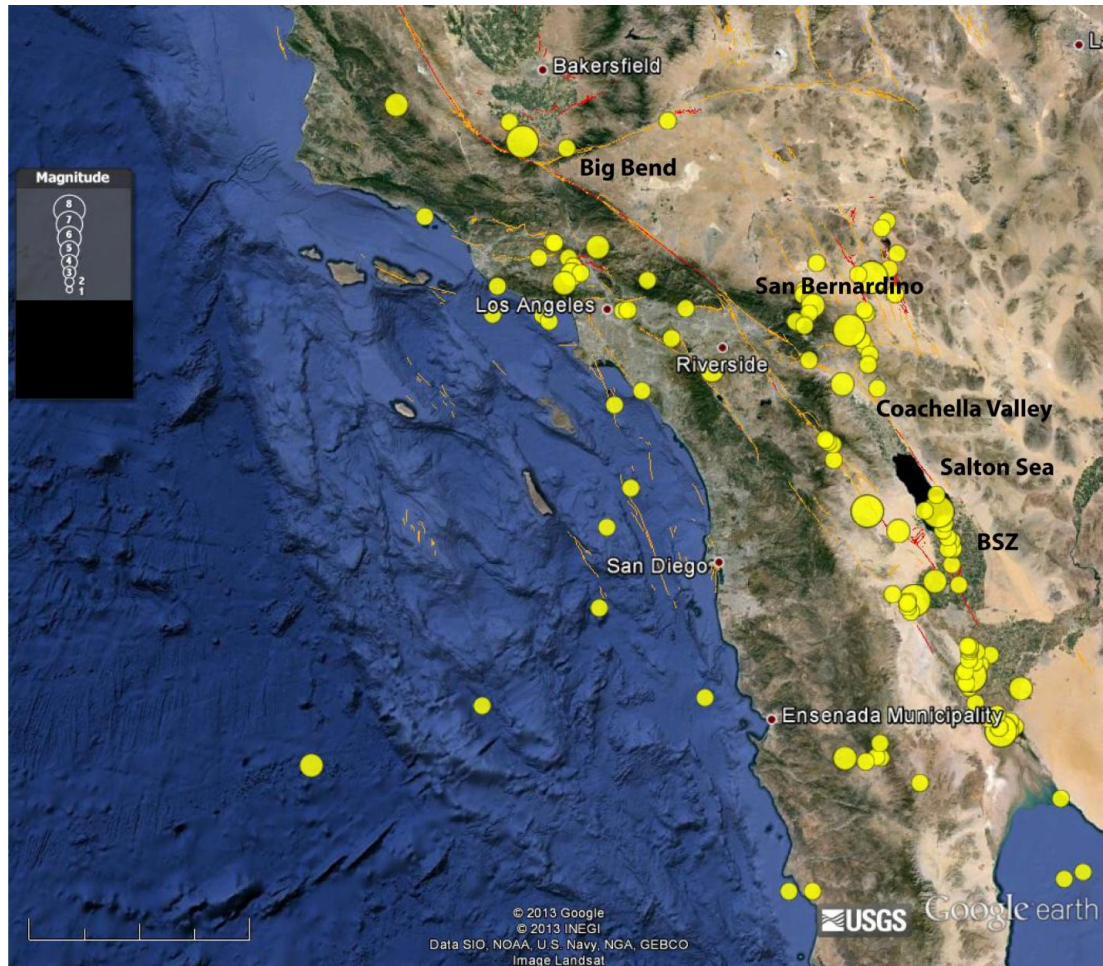
Figure 5.10.1: Map of recent earthquakes in the southern California and Baja California regions (1900-present; M >4). (U.S. Geological Survey, 2013).

Another means to gauge earthquake activity is using slip rate (Lindsey and

Fialko, 2013), or the speed at which one side of the fault, i.e. the Pacific plate, is

moving with respect to the other side, the North American plate. These rates are most

often determined through geodetic measurements or offset of both man-made and

geologic features. In Figure 5.10.2, the surface slip rates along the strike of the

southern SAFS are shown. San Bernardino (~25 mm/yr) and Salton Sea (~15 mm/yr)

segments contain higher values than the Coachella Valley segment (~10 mm/yr). The

Big Bend segment (not shown in figure 5.10.2) of the SAFS contains a high slip rate

of ~36 mm/yr (Schmalzle et al., 2006). In a crude sense, regions with higher slip rates

experience more and/or larger earthquakes.
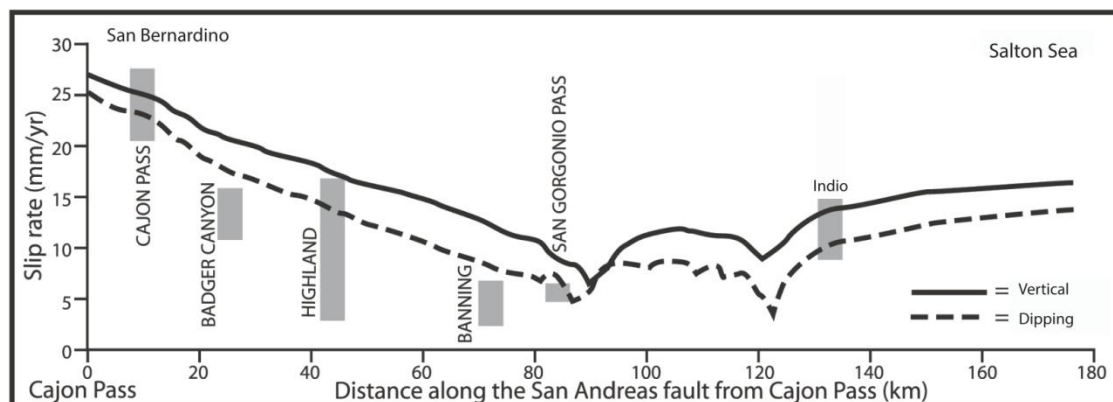
Figure 5.10.2: Plot modified from Yeats (2012) depicting the surface slip rates (mm/yr) along the southern SAFS southward from Cajon Pass.

Comparison of the seismic activity (as approximated by slip rate) with helium

isotope ratios and CO_2 fluxes show a generally positive correlation, as shown in

Figure 5.10.3. The higher the slip rate, the higher the helium isotope ratio and CO_2

flux rate. Salton Sea, San Bernardino, Coachella Valley, and Big Bend segments

contain helium isotope ratios of 2.23 R_A, 1.72 R_A, 0.97 R_A, and 3.52 R_A, respectively.

Salton Sea and San Bernardino have CO_2 flux rates of 324 x 10^5 mol CO_2/year/km and

198 x 10^5 mol CO_2/year/km respectively while Coachella Valley contains a lower flux

of 115 x 10^5 mol CO_2/year/km (all using method 1, see *section 5.8*). Additionally, the

Big Bend segment has a CO_2 flux rate of 659 x 10^5 mol CO_2/year/km. The only outlier

to these general trends is the Salton Sea where both the $^3He/^4He$ ratio and CO_2 flux are

higher than San Bernardino even though the slip rate is lower. This is most likely due to the magma-related degassing associated with the on-land rifting. The rift-related degassing elevates the helium isotope ratios and CO_2 fluxes, but not the SAFS slip rate.
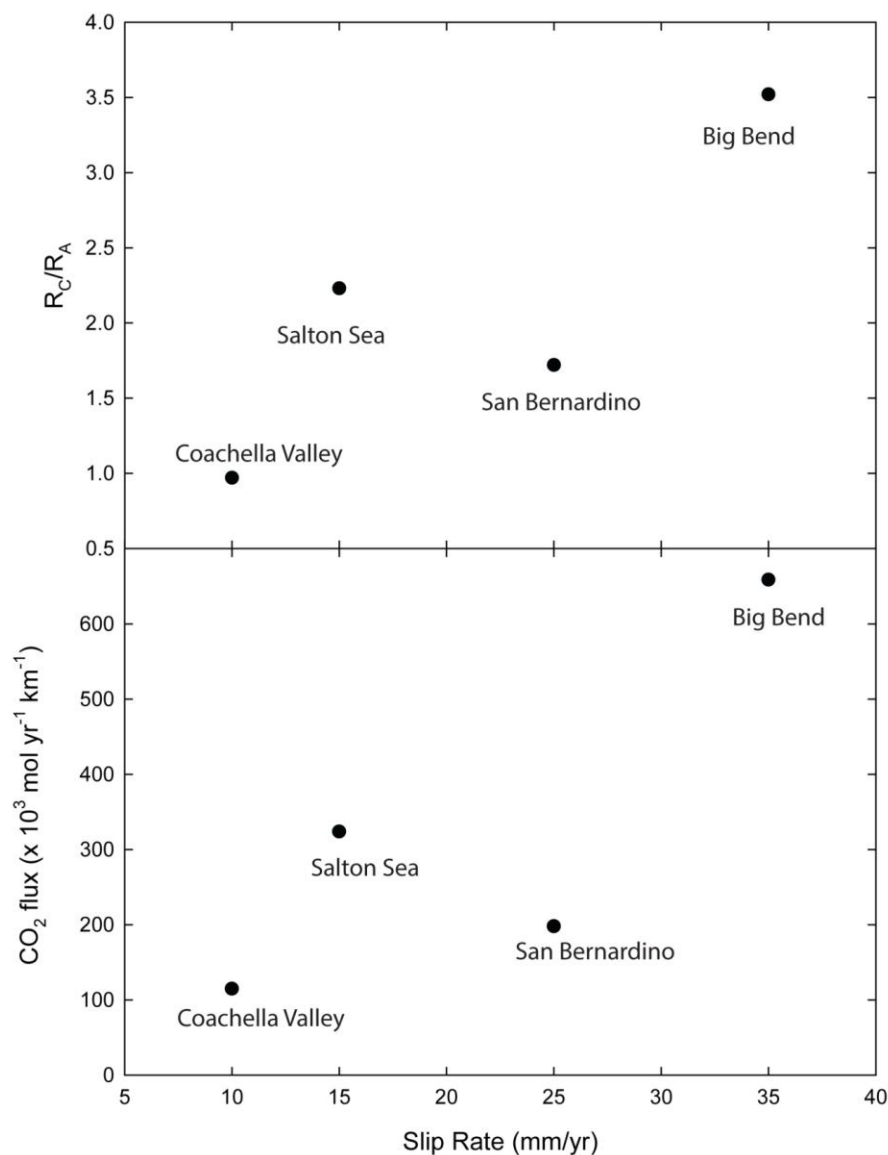
Figure 5.10.3: Slip rate of various segments of the southern SAFS versus helium isotope ratios corrected for air saturated water and air-bubble entrainment (R_C) normalized to ^{3}He/^{4}He ratio of air (R_A) and CO_2 fluxes through the SAFS.

6. Conclusions

Helium and carbon isotopic and abundance analysis was done on groundwater wells and hot springs sampled along the southern portion of the SAFS. The results of this study revealed that there is a mixture of both crustal and mantle-derived volatiles found within the groundwater systems along the SAFS. This study showed that wells close to SAFS (within 10 km) contain elevated ^{3}He/^{4}He ratios, but show large spatial variability. This spatial heterogeneity suggests that the helium distribution is greatly influenced by faults and overlying sediment. The elevated ^{3}He/^{4}He ratios are interpreted to be a consequence of mantle volatile upward flow through the SAFS. Carbon provenance was determined using two separate methods: binary and ternary mixing models. The ternary model seemed to be slightly more accurate in determining the endogenic, or mantle-derived, carbon.

Using the carbon and helium isotope and abundance data, fluid flux rates were calculated to compare to previous studies along the SAFS (Kennedy et al., 1997; Kulongoski et al., 2013). Upon analysis of the flux calculations, it was determined that the Salton Sea region is subject to more rift-related degassing while the Coachella Valley and San Bernardino regions are dominated by fault-related degassing. The southern portion of the SAFS represents a transition zone from rift- to fault-related degassing. Furthermore, after comparison with calculations made by Kulongoski et al. (2013), the southern portion of the SAFS sampled by this study accounts for 2.8% of the total carbon budget of the SAFS. Comparing the volatile flux per km per year of the various segments of the SAFS show that fault-related degassing does, indeed,

contribute a large amount of helium and carbon to the atmosphere. It shows that the SAFS should not be overlooked as a source of major volatile addition. Of course, it contributes a very small portion of total CO_2 worldwide, but it leaves a large potential for future research.

A chief concern for the southern California region is earthquake activity along the SAFS. One method to gauge earthquake activity can be to determine slip rates along the SAFS. When slip rate is compared with recent earthquake activity (1900-present) along the southern SAFS, there is a positive correlation. Additionally, when slip rate is compared with helium isotope ratios and CO_2 flux values there is also a positive correlation. So, using helium isotope and CO_2 data, potential hazardous fault segments along the SAFS can be identified.

7. Appendix

7.1. PHREEQC usage for Water Chemistry

To determine the saturation index (calcite) of the water samples, PHREEQC (Version 2; Parkhurst and Appelo, 1999), a computer program for speciation, batch-reaction, one-dimensional transport, and inverse geochemical calculations, was used. The program takes an input file (which can consist of the concentrations of dissolved ions, for instance), and according to the script written, will perform various aqueous geochemical speciation calculations. The input file has a basic table that includes the concentration (mg/L) of seven different constituents (Ca, Mg, Na, K, alkalinity as HCO_3, Cl, and SO_4) as well as the temperature and pH of the water. For the program to run correctly, PHREEQC must use a previously installed database.

As an example of an input file:

```
DATABASE C:\Program Files (x86)\Phreeqc\Databases\phreeqc.dat

SOLUTION_SPREAD
   -units   mg/L
Description          Temperature          pH       Ca       Mg       Na       K        Alkalinity Cl        S(6)
                                                                                       as HCO3
sample 1             72                   6.5      144.321  23.778   1066.3   63.980   260.885   1590      225
sample 2             etc.………………………………………………………………………………………………………………………………………………………………………
sample 3
etc.

SELECTED_OUTPUT
-file    allsamples.txt
-temperature
-percent_error
-activities  H+
-totals  Ca    Mg     Na      K       C(4)     Cl       S(6)
-molalities HCO3-
-saturation_indices  Calcite      Dolomite  Gypsum   CO2(g)


END
```

Figure 7.1.1: Example input file for PHREEQC.

With this input data, the program then creates an output text file that consists of concentrations totals of the constituents, molality of HCO_3, and the saturation indices of calcite, dolomite, gypsum and CO_2. The saturation index of calcite is the only data used for this study, however. A typical value of saturation index (seen in Table 2) would be 0.146, for example, seen at Cox Oasis in the Salton Sea. The value can be either positive or negative. Positive values represent a groundwater that is oversaturated with respect to calcite, and a solution undersaturated with respect to calcite is denoted by a negative saturation index (Hiscock, 2005).

7.2. Carbon provenance calculations using binary mixture

The measured total dissolved inorganic carbon (DIC) is comprised of carbon from two components: dissolution of carbonate (C_{carb}) from the aquifer and carbon not attributed to carbonate − external carbon (C_{ext}). The external carbon is further comprised of organic (C_{org}) and endogenic (C_{endo}) (i.e. deep) carbon (Chiodini et al., 2000; 2004; Crossey et al., 2009) (see Figure 7.2.1 for a general schematic).
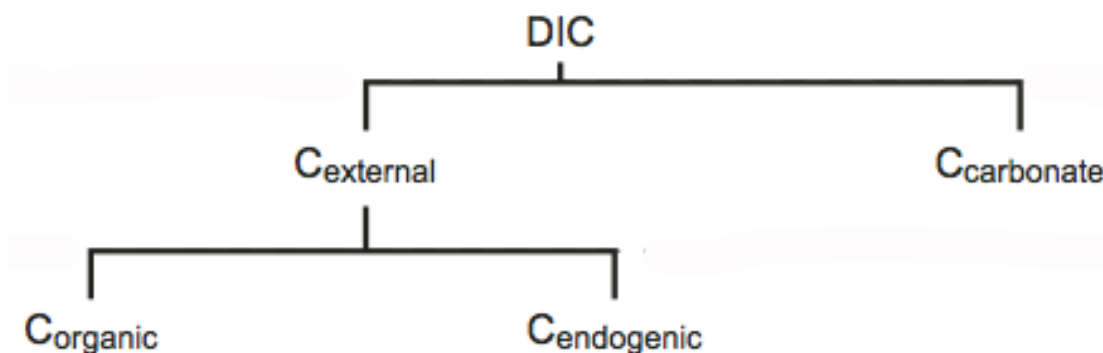
Figure 7.2.1: Constituents of DIC. Image adopted and modified from Chiodini et al. (2000, 2004), and Crossey et al. 2009

To resolve and calculate the various components of DIC (mol/L), the following equations were used:

$$C_{carb} = Ca + Mg - SO_4$$

Subtraction of C_{carb} from DIC allows calculation of the concentration of C_{ext}:

$$C_{ext} = DIC - C_{carb}$$

The carbon isotopic composition of external C can be calculated on mass balance grounds using the following equation:

$$(\delta^{13}C_{ext} \times C_{ext}) = (\delta^{13}C_{DIC} \times DIC) - (\delta^{13}C_{carb} \times C_{carb})$$

where $\delta^{13}C_{DIC}$ is the measured value, $\delta^{13}C_{carb} = 2$ ‰ (a typical value of Paleozoic carbonates; Veizer et al., 1999). Re-arranging the equation allows the percentage of C_{ext} to be calculated using the following equation.

$$\% \, C_{endo} = \frac{\delta^{13}C_{ext} - \delta^{13}C_{org}}{\delta^{13}C_{endo} - \delta^{13}C_{org}} \times 100$$

using the following assumptions: $\delta^{13}C_{org} = -35‰$ (Wycherly et al., 1999) and $\delta^{13}C_{endo} = -5‰$ (vs PDB) (Chidoni et al., 2000; Crossey et al., 2009) noting that $C_{org} + C_{endo} =$

C_{ext} (Crossey et al., 2009). Using the above calculations, a plot of $\delta^{13}C_{ext}$ versus C_{ext} can be created to determine percentage of C_{endo} contribution (Figure 7.2.2). As can be seen from the plot, mixing lines of various concentrations of C_{ext} (mol/L) are connected between two the fixed endmembers of $\delta^{13}C_{endo}$ (-5‰) and $\delta^{13}C_{org}$ (-35‰).
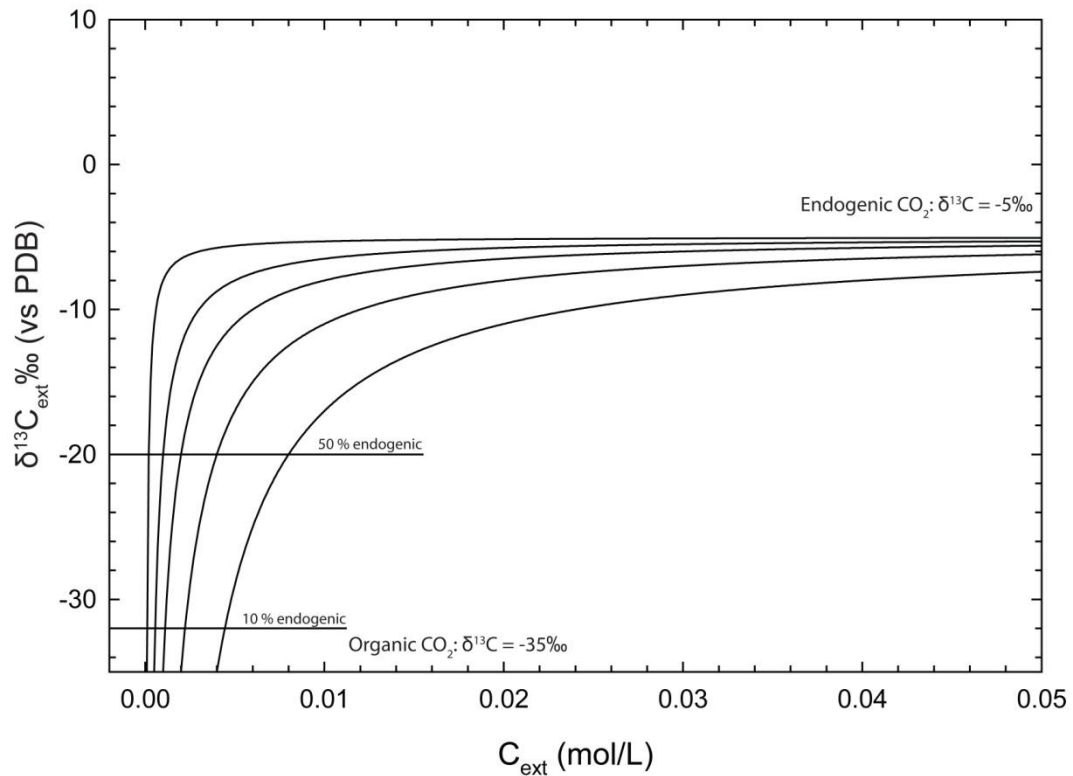
Figure 7.2.2: Plot of $\delta^{13}C_{ext}$ versus $C_{external}$ showing mixing lines between an endogenic (-5‰) and organic CO_2 endmember (-35‰) adopted from Chiodini et al. 2004 and Crossey et al. 2009.

The following sample, *Pacific Aquafarms*, is chosen as an illustrative example:

$C_{carb} = Ca + Mg - SO_4$: $0.0036 + 0.00097 - 0.0023 = 0.0022$ (mol/L)

$C_{ext} = DIC - C_{carb}$: $0.2701 - 0.0022 = 0.0098$ (mol/L)

Then to calculate the carbon isotopic composition of C_{ext}:

$(\delta^{13}C_{ext} \times C_{ext}) = (\delta^{13}C_{DIC} \times DIC) - (\delta^{13}C_{carb} \times C_{carb})$:

$$\frac{(-8.67\text{‰} \times 0.2701) - (+2\text{‰} \times 0.0022)}{0.0098} = -11.10 \text{ ‰}$$

Finally, to calculate the percentage contribution of endogenic carbon to DIC:

$$\% \text{ C}_{endo} = \frac{\delta^{13}\text{C}_{ext} - \delta^{13}\text{C}_{org}}{\delta^{13}\text{C}_{endo} - \delta^{13}\text{C}_{org}} \times 100:$$

$$\frac{-11.10 - (-35)}{-5 - (-35)} \times 100 = 79.7\%$$

Raw data and calculated values for all samples can be found in Table 3 (main text).

7.3. Carbon provenance using ternary mixture

A complementary approach to resolve DIC into component parts is illustrated in Figure 7.2.3 which plots $CO_2/^3He$ versus $\delta^{13}\text{C}_{ext}$. A mixture between mantle, organic sediment, and marine carbonate endmembers is used for the mixing model (Sano and Marty, 1995). Mantle fluids (M) contain $CO_2/^3He$ ratios at ~2×10^9 (Marty and Jambon, 1987) whereas crustal fluids are a mixture of organic sediment (S) and marine carbonates (L) at ~1×10^{13}. Typical mantle $\delta^{13}C$ values range from -9 to -4(‰ vs PDB) with an average of -6.5‰, while organic $\delta^{13}C$ values range from -40 to -20‰ and marine carbonates average 0.0 ± 2 ‰ (Sano and Marty, 1995). The proportion of CO_2 derived from each of the three endmembers (M, L, and S) can be calculated following the approach of Sano and Marty (1995) using the following three equations.

$$\left(\frac{^{13}\text{C}}{^{12}\text{C}}\right)_{Obs} = \left(\frac{^{13}\text{C}}{^{12}\text{C}}\right)_M M + \left(\frac{^{13}\text{C}}{^{12}\text{C}}\right)_L L + \left(\frac{^{13}\text{C}}{^{12}\text{C}}\right)_S S$$

$$\frac{1}{\left(\dfrac{^{12}C}{^{3}He}\right)_{Obs}} = \frac{M}{\left(\dfrac{^{12}C}{^{3}He}\right)_{M}} + \frac{L}{\left(\dfrac{^{12}C}{^{3}He}\right)_{L}} + \frac{S}{\left(\dfrac{^{12}C}{^{3}He}\right)_{S}}$$

with

$$M + S + L = 1$$

The mantle $\delta^{13}C$ value of -6.5‰ ($^{13}C/^{12}C = 0.01115$), marine carbonate $\delta^{13}C$ value of 0‰ ($^{13}C/^{12}C = 0.01122$), and organic $\delta^{13}C$ value of -35‰ ($^{13}C/^{12}C = 0.01083$) were used in the calculation. The calculations of the samples from this study are given in Table 3. The implications of calculations of carbon provenance and Figures 7.2.2 and 7.3.1 are discussed further in *section 5.4*.
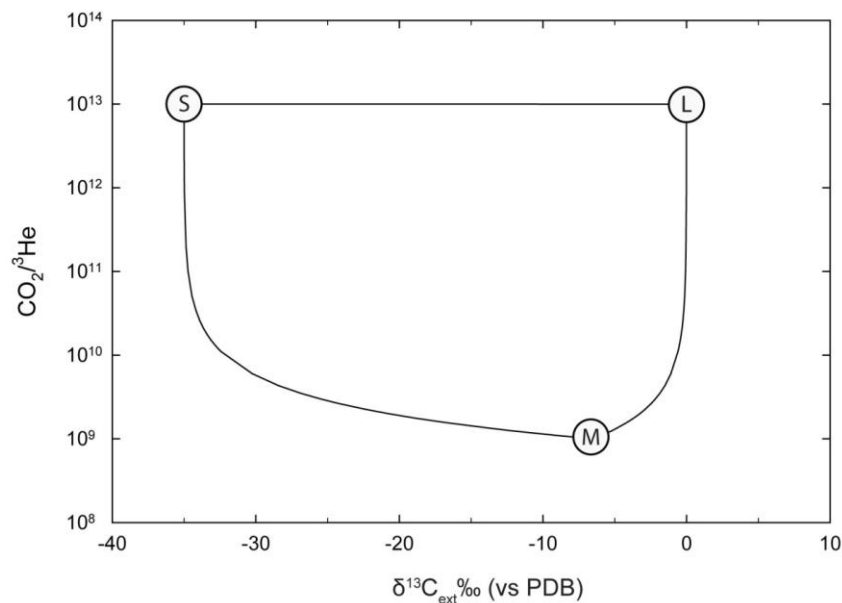
Figure 7.3.1: Plot of organic sediment "S", mantle "M", and marine carbonate "L" endmembers with corresponding binary mixing lines. Adopted from Sano and Marty (1995) and Kulongoski et al. (2013).

References

Andrews, J. N. (1985). The isotopic composition of radiogenic helium and its use to study groundwater movement in confined aquifers. *Chemical Geology*, *49*(1), 339-351.

Barry, P.H., et al., Helium and carbon isotope systematics of cold "mazuku" CO2 vents and hydrothermal gases and fluids from Rungwe Volcanic Province, southern Tanzania, Chem. Geol. (2012), doi:10.1016/j.chemgeo.2012.07.003

Bethke, C. M., Torgersen, T., & Park, J. (2000). The "age" of very old groundwater: insights from reactive transport models. *Journal of Geochemical Exploration*, *69*, 1-4.

Bianchi, D., Sarmiento, J. L., Gnanadesikan, A., Key, R. M., Schlosser, P., & Newton, R. (2010). Low helium flux from the mantle inferred from simulations of oceanic helium isotope data. *Earth and Planetary Science Letters*, *297*(3), 379-386.

Blisniuk, K., Rockwell, T., Owen, L. A., Oskin, M., Lippincott, C., Caffee, M. W., & Dortch, J. (2010). Late Quaternary slip rate gradient defined using high-resolution topography and 10Be dating of offset landforms on the southern San Jacinto Fault zone, California. *Journal of Geophysical Research: Solid Earth (1978–2012)*, *115*(B8).

C.J., Wieler, R. (Eds.), Noble Gases in Geochemistry and Cosmochemistry. Mineralogical Society of America, Washington, pp. 247–318.

Carl E. Johnson and David M. Hadley. (1975) Tectonic implications of the Brawley earthquake swarm, Imperial Valley, California. Bulletin of the Seismological Society of America, August 1976, v. 66, p.1133-1144.

Chiodini, G., Frondini, F., Cardellini, C., Parello, F., & Peruzzi, L. (2000). Rate of diffuse carbon dioxide Earth degassing estimated from carbon balance of regional aquifers: the case of central Apennine, Italy. *Journal of Geophysical Research: Solid Earth (1978–2012)*, *105*(B4), 8423-8434.

Chiodini, G., Cardellini, C., Amato, A., Boschi, E., Caliro, S., Frondini, F., & Ventura, G. (2004). Carbon dioxide Earth degassing and seismogenesis in central and southern Italy. *Geophysical Research Letters*, *31*(7), L07615.

Clarke, W.B., Jenkins, W.J., Top, Z. (1976). Determination of tritium by mass spectrometric measurement of He-3. *International Journal of Applied Radiation and Isotopes,* 27, 515–522.

Clark, Ian D., and P. Fritz. *Environmental Isotopes in Hydrogeology*. Boca Raton, FL:

CRC/Lewis, 1997.

Crossey, L. J., Karlstrom, K. E., Springer, A. E., Newell, D., Hilton, D. R., & Fischer, T. (2009). Degassing of mantle-derived CO2 and He from springs in the southern Colorado Plateau region—Neotectonic connections and implications for groundwater systems. *Geological Society of America Bulletin*, *121*(7-8), 1034-1053.

Danskin, W. R., McPherson, K. R., & Woolfenden, L. R. (2006). *Hydrology, description of computer models, and evaluation of selected water-management alternatives in the San Bernardino area, California*. U. S. Geological Survey.

Dickson, A. G., Afghan, J. D., & Anderson, G. C. (2003). Reference materials for oceanic CO_2 analysis: a method for the certification of total alkalinity. *Marine Chemistry*, *80*(2), 185-197.

Domenico, P. A., & Schwartz, F. W. (1998). *Physical and chemical hydrogeology* (Vol. 44). New York: Wiley.

Dunai, T. J., & Baur, H. (1995). Helium, neon, and argon systematics of the European subcontinental mantle: Implications for its geochemical evolution.*Geochimica et Cosmochimica Acta*, *59*(13), 2767-2783.

Dunai, T.J., Porcelli, D., 2002. Storage and transport of noble gases in the subcontinental lithosphere. In: Porcelli, D., Ballentine, C.J., Wieler, R. (Eds.), Noble Gases in Geochemistry and Cosmochemistry: Rev. Mineral. Geochem. Mineral. Soc. Am., vol. 47 Washington, DC, pp. 371–409.

Dutcher, L. C., & Garrett, A. A. (1963). *Geologic and hydrologic features of the San Bernardino area, California*. US Government Printing Office.

Fetter, C.W. Jr., 1980. Applied Hydrogeology. Chas. Merrill Publishing, Columbus, OH.

Fuis, G. S. Kohler, W. M. (1984). Crustal structure and tectonics of the Imperial Valley region, California, in *The Imperial Basin—Tectonics, Sedimentation, and Thermal Aspects*, Rigsby, C. A. , Editor Soc. of Econ. Pal. and Min. (SEPM), Pacific Section, 1- 13.

Fuis, G. S. Mooney, W. D. Healy, J. H. McMechan, G. A. Lutter, W. J. (1982).Crustal structure of the Imperial Valley region, California, in *The Imperial Valley earthquake of October 15, 1979*, *U.S. Geol. Surv. Profess. Paper 1254*,25- 49.

Graham, D. W. (2002). Noble gas isotope geochemistry of mid-ocean ridge and ocean island basalts: Characterization of mantle source reservoirs. *Reviews in Mineralogy and Geochemistry*, *47*(1), 247-317.

Goldrath, D. A., Wright, M. T., & Belitz, K. (2009). *Ground-water Quality Data in the Coachella Valley Study Unit, 2007: Results from the California GAMA Program*. US Geological Survey.

Hautman, Daniel P and Munch, David J. (1997). National Method 300.1: Determination of Inorganic Anions in Drinking Water by Ion Chromatography.

Hill, D. P., Eaton, J. P., & Jones, L. M. (1990). Seismicity, 1980-86. *United States Geological Survey, Professional Paper;(USA)*, *1515*.

Hilton, D. R., Macpherson, C. G., & Elliott, T. R. (2000). Helium isotope ratios in mafic phenocrysts and geothermal fluids from La Palma, the Canary Islands (Spain): implications for HIMU mantle sources. *Geochimica et Cosmochimica Acta*, *64*(12), 2119-2132.

Hiscock, K. (2009). *Hydrogeology: principles and practice*. Wiley.com.

Janney, P. E., & Castillo, P. R. (1996). Basalts from the Central Pacific Basin: Evidence for the origin of Cretaceous igneous complexes in the Jurassic western Pacific. *Journal of geophysical research*, *101*(B2), 2875-2893.

Johnson, Carl Edward. (1979). *I. CEDAR -- an approach to the computer automation of short-period local seismic networks. II. Seismotectonics of the Imperial Valley of southern California*. Dissertation (Ph.D.), California Institute of Technology. http://resolver.caltech.edu/CaltechTHESIS:04232010-074317474

Kulongoski, J. T., & Hilton, D. R. (2002). A quadrupole-based mass spectrometric system for the determination of noble gas abundances in fluids.*Geochemistry, Geophysics, Geosystems*, *3*(6), 1-10.

Kulongoski, J.T. and Hilton, D.R. (2011). Applications of groundwater helium. In: M. Baskaran (Editor), Handbook of Environmental Isotope Geochemistry. Springer-Verlag, pp. 285-304.

Kulongoski, J. T., Hilton, D. R., Barry, P. H., Esser, B., Hillegonds, D., & Belitz, K. (2013). Volatile fluxes through the Big Bend section of the San Andreas Fault, California: Helium and carbon-dioxide systematics. *Chemical Geology*.

Lindsey, E. O., & Fialko, Y. (2013). Geodetic slip rates in the southern San Andreas Fault system: Effects of elastic heterogeneity and fault geometry.*Journal of Geophysical Research: Solid Earth*.

Lupton, J. E., Klinkhammer, G. P., Normark, W. R., Haymon, R., Macdonald, K. C., Weiss, R. F., & Craig, H. (1980). Helium-3 and manganese at the 21 N East Pacific Rise hydrothermal site. *Earth and Planetary Science Letters*,*50*(1), 115-127.

Marty, B., & Jambon, A. (1987). C^3He in volatile fluxes from the solid Earth: implications for carbon geodynamics. *Earth and Planetary Science Letters*, *83*(1), 16-26.

Mazzini, A., Svensen, H., Etiope, G., Onderdonk, N., & Banks, D. (2011). Fluid origin, gas fluxes and plumbing system in the sediment-hosted Salton Sea Geothermal System (California, USA). *Journal of Volcanology and Geothermal Research*, *205*(3), 67-83.

Methods of Analysis by the U.S. Geological Survey, San Diego Laboratory**.** Determination of Fluoride, Chloride, Nitrite, Bromide, Nitrate, Orthophosphate, and Sulfate by Ion Chromatography. June 2008.

Morton, D. M., & Matti, J. C. (1993). Extension and contraction within an evolving divergent strike-slip fault complex: The San Andreas and San Jacinto fault zones at their convergence in southern California. *Mem. Geol. Soc. Am*,*178*, 217-230.

Muffler, L. P., & White, D. E. (1969). Active metamorphism of upper Cenozoic sediments in the Salton Sea geothermal field and the Salton Trough, southeastern California. *Geological Society of America Bulletin*, *80*(2), 157-182.

Nadeau, R. A. (1997). The Water Seekers – 4th Edition, revised, pgs. 139 – 232, Crest Publishers, Santa Barbara, California.

Nur, A. M. O. S., & Walder, J. O. S. E. P. H. (1990). Time-dependent hydraulics of the Earth's crust. *The role of fluids in crustal processes*, 113-127.

Onderdonk, N., Mazzini, A., Shafer, L., & Svensen, H. (2011). Controls on the geomorphic expression and evolution of gryphons, pools, and caldera features at hydrothermal seeps in the Salton Sea Geothermal Field, southern California.*Geomorphology*, *130*(3), 327-342.

O'Nions, R. K., & Oxburgh, E. R. (1988). Helium, volatile fluxes and the development of continental crust. *Earth and Planetary Science Letters*, *90*(3), 331-347.

Ozima, M., & Podosek, F. A. (2002). *Noble gas geochemistry*. Cambridge University Press.

Parkhurst, D. L., & Appelo, C. A. J. (1999). User's guide to PHREEQC (Version 2): A computer program for speciation, batch-reaction, one-dimensional transport, and inverse geochemical calculations.

Pineau, F., & Javoy, M. (1983). Carbon isotopes and concentrations in mid-oceanic ridge basalts. *Earth and Planetary Science Letters*, *62*(2), 239-257.

Planert M, Williams JS (1995) Ground water atlas of the United States: California and Nevada. US Geol Surv Atlas 730-B.

Proctor, R. J. (1968). *Geology of the Desert Hot Springs – Upper Coachella Valley Area,California*, 50 pgs., California Division of Mines and Geology, Special Report 94, San Francisco, California.

Robinson, P. T., Elders, W. A., & Muffler, L. J. P. (1976). Quaternary volcanism in the Salton Sea geothermal field, Imperial Valley, California. *Geological Society of America Bulletin*, *87*(3), 347-360.

Roeloffs, E. A., Danskin, W. R., Farrar, C. D., Galloway, D. L., Hamlin, S. N., Quilty, E. G., ... & Woodcock, D. E. (1995). Hydrologic effects associated with the June 28, 1992. *Landers, California, earthquake sequence: US Geological Survey Open-File Report*, 95-42.

Rogie, J. D., Kerrick, D. M., Chiodini, G., & Frondini, F. (2000). Flux measurements of nonvolcanic CO_2 emission from some vents in central Italy.*Journal of Geophysical Research: Solid Earth (1978–2012)*, *105*(B4), 8435-8445.

Salton Sea Quadrangle. California Geological Survey, Geologic Atlas of California Map No. 013, 1:250,000 scale. Compilation by: Charles W. Jennings, 1967

Sano, Y., & Marty, B. (1995). Origin of carbon in fumarolic gas from island arcs.*Chemical Geology*, *119*(1), 265-274.

Santa Ana Quadrangle. California Geological Survey, Geologic Atlas of California Map No. 019, 1:250,000 scale. Compilation by: Thomas H. Rogers, 1965

Sano, Y., & Marty, B. (1995). Origin of carbon in fumarolic gas from island arcs.*Chemical Geology*, *119*(1), 265-274.

Schmalzle, G., Dixon, T., Malservisi, R., & Govers, R. (2006). Strain accumulation across the Carrizo segment of the San Andreas Fault, California: Impact of laterally varying crustal properties. *Journal of geophysical research*,*111*(B5), B05403.

Torgersen, T., & O'Donnell, J. (1991). The degassing flux from the solid earth: release by fracturing. *Geophysical Research Letters*, *18*(5), 951-954.

U.S. Geological Survey, 2013. Quaternary Faults in Google Earth. accessed January 25, 2013, at http://earthquake.usgs.gov/hazards/qfaults/google.php

U.S. Geological Survey, 2013. Historic United States earthquakes: USGS Earthquake Hazards Program website. accessed September 6, 2013, at http://earthquake.usgs.gov/earthquakes/?source=sitenav

Veizer, J., Ala, D., Azmy, K., Bruckschen, P., Buhl, D., Bruhn, F., & Strauss, H. (1999). $^{87}Sr/^{86}Sr$, $\delta^{13}C$ and $\delta^{18}O$ evolution of Phanerozoic seawater. *Chemical Geology*, *161*(1), 59-88.

Wallace, R. E. (1990). *The San Andreas fault system, California*. Washington, DC: US Government Printing Office.

Weiss, R. F. (1968), Piggyback sampler for dissolved gas studies on sealed water samples, Deep Sea Res., 15, 695-699.

Weiss, R. F. (1971). Solubility of helium and neon in water and seawater. *Journal of Chemical & Engineering Data*, *16*(2), 235-241.

Woolfenden, L. R., & Kadhim, D. (1997). Geohydrology and water chemistry in the Rialto-Colton Basin, San Bernardino County, California. *Water-resources investigations report*.

Yeats, R. (2012). *Active faults of the world*. (pp. 79-137). New York: Cambridge University Press.